MNRAS **000**, 000–000 (0000) Preprint 24 November 2016 Compiled using MNRAS LATEX style file v3.0

Circumstellar Dust, PAHs, and Stellar Populations in Early-Type Galaxies: Insights from *GALEX* and *WISE*

Gregory V. Simonian[1⋆] and Paul Martini[1,2]
[1] *Department of Astronomy, The Ohio State University, 140 West 18th Avenue, Columbus, OH 43210, USA*
[2] *Center for Cosmology and AstroParticle Physics (CCAPP), The Ohio State University, 191 W. Woodruff Ave., Columbus, OH 43210, USA*

arXiv:1603.09345v2 [astro-ph.GA] 22 Nov 2016

24 November 2016

ABSTRACT

A majority of early-type galaxies contain interstellar dust, yet the origin of this dust, and why the dust sometimes exhibits unusual polycyclic aromatic hydrocarbon (PAH) ratios, remains a mystery. If the dust is internally produced, it likely originates from the large number of asymptotic giant branch stars associated with the old stellar population. We present *GALEX* and *WISE* elliptical aperture photometry of ~ 310 early-type galaxies with Spitzer mid-infrared spectroscopy and/or ancillary data from ATLAS^{3D}, to characterize their circumstellar dust and the shape of the radiation field that illuminates the interstellar PAHs. We find that circumstellar dust is ubiquitous in early-type galaxies, which indicates some tension between stellar population age estimates and models for circumstellar dust production in very old stellar populations. We also use dynamical masses from ATLAS^{3D} to show that *WISE* W1 (3.4 μm) mass-to-light ratios are consistent with the initial mass function variation found by previous work. While the stellar population differences in early-type galaxies correspond to a range of radiation field shapes incident upon the diffuse dust, the ratio of the ionization-sensitive 7.7μm to 11.3μm PAH feature does not correlate with the shape of the radiation field, nor to variations with the size-sensitive 11.3μm to 17μm ratio. The 7.7μm to 11.3μm PAH ratio does tend to be smaller in galaxies with proportionally greater H_2 emission, which is evidence that processing of primarily smaller grains by shocks is responsible for the unusual ratios, rather than substantial differences in the overall PAH size or ionization distribution.

Key words: galaxies: elliptical and lenticular, cD – infrared: galaxies – ultraviolet: galaxies – galaxies: stellar content

1 INTRODUCTION

While early-type galaxies (ETGs) were historically associated with uniformly old stellar populations and no cold interstellar medium (ISM), forty years of multiwavelength observations have demonstrated that view is too simplistic. Instead, many ETGs have a complex, multiphase ISM, often with a mixture of cold (Knapp et al. 1985; Wardle & Knapp 1986), warm (Caldwell 1984; Phillips et al. 1986; Sadler 1987), and hot (Forman et al. 1985; Canizares et al. 1987) gas. Improved angular resolution has also led to the detection of dust lanes in many ETGs (Sadler & Gerhard 1985; Sparks et al. 1985; Ebneter et al. 1988; Veron-Cetty & Veron 1988; Goudfrooij et al. 1994), and observations in the far-infrared (FIR) indicated that many ETGs contain a diffuse, cold dust component (Jura et al. 1987; Knapp et al. 1989; Goudfrooij & de Jong 1995; Bregman et al. 1998). Mid-Infrared (MIR) observations from the *Infrared Space Observatory* (*ISO*) satellite found flux in excess of expectations for the stellar population of many ETGs, which was postulated to arise from either Polycyclic Aromatic Hydrocarbon (PAH) or Very Small Grain (VSG) emission (Madden et al. 1999; Ferrari et al. 2002; Xilouris et al. 2004; Pahre et al. 2004). The existence of these small grains was surprising because of their short lifetimes in hot plasma (Draine & Salpeter 1979; Dwek & Arendt 1992), and so the origin of these grains is hotly debated.

MIR spectroscopy of individual PAH features in ETGs indicated that the relative strengths of short-wavelength and long-wavelength PAH features were often vastly reduced compared to the same features in star-forming galaxies (Kaneda et al. 2005). Proposed physical conditions which could lead to the relatively weaker short-wavelength features include a grain population dominated by neutral rather than

⋆ E-mail: simonian@astronomy.ohio-state.edu

© 0000 The Authors

ionized PAHs, and a larger grain size distribution compared to star-forming galaxies (Draine & Li 2007).

An explanation for both the existence of PAHs and their anomalous line ratios in ETGs has proven elusive. Kaneda et al. (2008) found that PAH emission is uncorrelated with stellar emission, and suggested that larger neutral PAHs were externally accreted through mergers. Alternatively, Vega et al. (2010) posited that PAHs are produced by carbon stars formed in a minor star-forming event, and that shocks with the ambient ISM then preferentially destroyed the small grains.

For galaxies without interstellar dust, we get a direct view of the MIR emission of the stellar population, which makes these galaxies well-suited to test Stellar Population Synthesis (SPS) models. They are representative of old stellar populations with little ongoing star formation (Yi et al. 2005; Kaviraj et al. 2007; Temi et al. 2009; Shapiro et al. 2010), and negligible extinction due to dust. We will use them to test stellar models for the evolved giant stars that dominate their light, especially the substantial progress on the Thermally Pulsating Asymptotic Giant Branch (TP-AGB) phase over the last decade (Marigo et al. 2008; Girardi et al. 2010; Cassarà et al. 2013; Marigo et al. 2013; Rosenfield et al. 2014). This phase is critical as the stars can contribute a significant amount of the integrated flux in the infrared (Maraston 2005; Kelson & Holden 2010; Melbourne et al. 2012; Conroy 2013; Melbourne & Boyer 2013).

Previous studies of AGB stars have shown that circumstellar dust is necessary to adequately describe their spectra in the MIR (Bedijn 1987; van Loon et al. 1999; Trams et al. 1999). However, the inclusion of circumstellar dust within SPS models has been difficult, and only a few models incorporate dusty AGB stars into their spectral libraries (Bressan et al. 1998; Silva et al. 1998; Marigo et al. 2008; Villaume et al. 2015). The expansion of MIR observations provide new opportunities to compare these circumstellar dust models to real stellar populations (e.g. Norris et al. 2014; Villaume et al. 2015).

It is difficult to compare circumstellar dust models to data in active star-forming galaxies because the circumstellar dust emission is often dwarfed by emission from dust in the diffuse ISM. For our sample of passive early-type galaxies with much less interstellar dust, the circumstellar component can be observed in the MIR (beyond about 10 μm). Excess flux associated with circumstellar dust has been identified in a number of studies of galaxies without evidence for interstellar dust (Bressan et al. 1998; Athey et al. 2002; Martini et al. 2013).

The MIR region from 3–5 μm dominated by photospheric emission is valuable for stellar mass measurements. Since low-mass stars contain most of the stellar mass of a galaxy, observations at these wavelengths are more robust to variations in metallicity, star formation history (SFH), and star formation rate (SFR; Meidt et al. 2014). Results from SPS models have traditionally been the only way to measure the stellar masses of large numbers of galaxies. Alternative mass estimates were recently released by ATLAS^{3D} for a volume-limited sample of 260 ETGs closer than 42 Mpc with $M_* \gtrsim 6 \times 10^9 M_\odot$. Cappellari et al. (2013) derived dynamical masses for these galaxies using r-band photometry, SAURON integral-field unit (IFU) spectroscopy, and dynamical models based on the Jeans equations. They then obtained stellar masses by subtracting a Navarro-Frenk-White (NFW) halo; which yielded stellar masses with assumptions independent from SPS models.

We use MIR data from the *WISE* satellite, which observed the entire sky in four MIR bands: W1 (3.4 μm), W2 (4.6 μm), W3 (12 μm), and W4 (22 μm) (see Wright et al. (2010) for further details). The first two bands are similar to the *Spitzer* Infrared Array Camera (IRAC) [3.6] and [4.5] bands, and the W4 band is similar to the Multiband Imaging Photometer on *Spitzer* (MIPS) 24 μm band. In typical galaxies, the W1 and W2 bands are expected to trace the evolved stellar population; the W3 band will contain significant PAH features; and the W4 band will be dominated by continuum emission from hot dust grains (e.g. Jarrett et al. 2013). Due to the all-sky coverage of *WISE*, all sufficiently bright ETGs can be studied in the MIR, a substantial increase over previous targeted surveys. This wide coverage will yield valuable demographic data about the stellar populations, circumstellar dust, and PAHs in ETGs, as well as identify promising targets for future study with targeted missions.

We also include UV photometry from the *GALEX* satellite to measure the shape of the radiation field incident on any PAHs that may be present. *GALEX* observed 63% of the sky to a depth of at least $m_{AB} = 20$ mag in the FUV (1516Å) and NUV (2267Å) bands, with a resolution of about 4.25″ and 5.25″ respectively (see Morrissey et al. (2005) and Martin et al. (2005) for further details).

In this paper, we distinguish between "interstellar" and "circumstellar" dust as follows: "circumstellar" dust resides within the stellar winds of AGB stars while "interstellar" dust resides within the diffuse ISM. Circumstellar dust is intrinsically connected to the stellar population, which makes it a valuable extension to Stellar Population Synthesis models. Meanwhile, interstellar dust is often uncorrelated with the stellar population and often dominates the IR emission when it is present.

Our paper is organized as follows: the next section of this paper contains a description of our samples of ETGs. Section 3 describes how we performed aperture photometry on both *WISE* and *GALEX* images and how we distinguish between galaxies with and without diffuse dust. In Section 4, we calculate stellar mass-to-light ratios for W1 from ATLAS^{3D} dynamical masses and compare them to mass-to-light ratios predicted by SPS models. We also compare models of circumstellar dust to our data, and use these to jointly constrain stellar ages and the masses of stars that produce circumstellar dust, as well as investigate the extent to which circumstellar dust can contaminate measurements of the SFR as measured from MIR indicators. Section 5 combines *GALEX* and *WISE* photometry with *Spitzer* Infrared Spectrograph (*Spitzer*-IRS) spectroscopy from previous works to investigate the properties of PAHs and their environments in ETGs. We also comment on the use of *WISE* photometry to determine the MIR properties of ETGs. We summarize our results in Section 6.

2 SAMPLES

We use MIR and UV photometry to study circumstellar and interstellar dust in ETGs. Our sample is drawn from two recent, comprehensive studies of ETGs: the characterizations of interstellar dust in ETGs with *Spitzer*-IRS spectra (Rampazzo et al. 2013), and the stellar population and dynamical study from the ATLAS^{3D} survey.

2.1 RSA *Spitzer*-IRS Atlas

The Revised Shapley-Ames (RSA) catalog is a canonical collection of bright, well-studied, nearby galaxies. Rampazzo et al. (2013) constructed their RSA *Spitzer*-IRS atlas by cross-matching the E–S0 galaxies from the RSA catalog with *Spitzer*-IRS observations available in the *Spitzer* Heritage Archive (SHA). This sample consists of 91 ETGs, including 56 E-type, 27 S0-type, and 8 mixed E/S0+S0/E-type galaxies; their properties are given in Table 1. Rampazzo et al. (2013) uniformly reprocessed and analyzed all of these spectra and measured line intensities for each of the detected emission lines.

Rampazzo et al. (2013) classified galaxies according to the Panuzzo et al. (2011) classification scheme for MIR spectra. A summary of the classification scheme is as follows: Class-0 galaxies are completely passive, that is apart from a few broad circumstellar dust features (Bressan et al. 1998), they have no emission lines in the MIR. These galaxies have spectra consistent with only an old stellar population. Class-1 galaxies have emission features in their spectra, but no PAH features. Class-2 and Class-3 galaxies are those with anomalous and normal PAH features, respectively; they will be the primary focus of this work. Finally, Class-4 galaxies have a hot dust continuum.

2.2 The ATLAS^{3D} Sample

The ATLAS^{3D} project surveyed a volume-limited sample within 42 Mpc of morphologically-selected early-type galaxies with $M_K < -21.5$ mag (Cappellari et al. 2011). This sample contains 260 ETGs: 68 E galaxies and 192 S0 galaxies (see Table 1). The extensive data available for the ATLAS^{3D} sample includes Sloan Digital Sky Survey (SDSS) *ugriz* photometry (Abazajian et al. 2009; Scott et al. 2013), observations with the SAURON IFU spectrograph (Cappellari et al. 2011), 21 cm emission observations (Serra et al. 2012), and ^{12}CO J=1–0 and J=2–1 observations (Alatalo et al. 2013). These data are available from the ATLAS^{3D} website[1].

The data collected for the ATLAS^{3D} sample, combined with extensive dynamical and stellar population modeling, has resulted in a wealth of valuable measurements. Some relevant observational results include the presence of optical dust features (Krajnović et al. 2011), surface brightness profiles (Scott et al. 2013), and luminosities in the r-band (Cappellari et al. 2013). We use their stellar population parameters derived from both SSP models and reconstructed SFH models (McDermid et al. 2015) to evaluate circumstellar dust models.

Finally, the dynamical analysis and modeling by Cappellari et al. (2013) include dynamical mass-to-light ratios derived by fitting model $\langle v_{los}^2 \rangle^{1/2}$ to V_{RMS} measurements. These were derived from Jeans Anisotropic Multi-gaussian expansion (JAM) modeling (Cappellari 2008). The output from these fits include stellar mass-to-light ratios derived by simultaneously fitting an NFW halo (Navarro et al. 1996) and a separate stellar distribution constrained by the observed surface brightness profile (Cappellari et al. 2013).

3 DATA PROCESSING

We chose to perform all aperture photometry with the standard aperture used by the Two Micron All-Sky Survey (2MASS) Extended Source Catalog (XSC)[2]: the K_s=20 mag arcsec^2 isophote (hereafter K20). This isophote corresponds roughly to 1σ of the typical background noise in the K_s images. Despite the fact that the K20 isophote underrepresents the "total" flux by $\sim$ 10–20%, it provides the most reproducible measurement of a galaxy's flux[3]. There are also 2MASS JHK_s measurements of the entire sample in this same aperture. The sizes of apertures for selected galaxies are shown in Fig. 1.

Due to PSF differences between the 2MASS and *WISE* surveys, the effective shape of the aperture needs to be corrected in order for the isophotes in the different beams to match[4]. Because the *WISE* W4 beam is larger and more circular than the beams for the other three *WISE* bands, the W4 aperture is a different size and shape from the rest. For all but three objects, this adjustment was performed by the *WISE* pipeline, which generates a corrected aperture any time a 2MASS XSC object is centered within 2″ of the *WISE* source. For the three objects whose centers in the two surveys are separated by more than 2″, we generated a matched aperture manually. We calculated these apertures by binning the ATLAS^{3D} sample by 2MASS axis ratio, and interpolated the adjusted *WISE* semimajor axis and axis ratio to the object. *GALEX* apertures were not adjusted because the PSF differences are less important. The photometry parameters for all of the galaxies in our sample are given in Table 1.

3.1 *WISE*

We measured aperture photometry on the *WISE* Atlas images. These are coadded images available as high-level data products. The details of the image construction and calibration are described in the *WISE* explanatory supplement[5].

There are presently two recommended data releases: All-Sky and AllWISE. The AllWISE release is more precise and sensitive because it incorporates observations from the post-cryo mission into the standard mission observations, among other improvements. However, inclusion of post-cryo observations decreases the saturation limit of the images, and hence decreases accuracy for bright objects. We therefore used All-Sky images for objects with saturated pixels,

[1] http://www-astro.physics.ox.ac.uk/atlas3d/

[2] http://www.ipac.caltech.edu/2mass/releases/allsky/

[3] http://www.ipac.caltech.edu/2mass/releases/allsky/doc/sec4_5a5.html

[4] http://wise2.ipac.caltech.edu/docs/release/allsky/expsup/sec4_4c.ht

[5] http://wise2.ipac.caltech.edu/docs/release/allsky/expsup/index.html

Table 1. Aperture photometry parameters for galaxies in the ATLAS^{3D} and Rampazzo et al. (2013) samples

Galaxy (1)	Morph (2)	D (3)	S (4)	a_{W1} (5)	a_{W4} (6)	b/a_{W1} (7)	b/a_{W4} (8)	PA (9)	Survey (10)	NUV Tile (11)	FUV Tile (12)
IC0560	S0-a	27.2	A	31.1	35.23	0.47	0.56	10	AllWISE	MISDR1_24342_0266	MISDR1_24342_02
IC0598	S0-a	35.3	A	31.4	37.39	0.43	0.55	10	AllWISE	–	–
IC0676	S0-a	24.6	A	37.9	40.93	0.62	0.62	-20	AllWISE	GI4_042019_J111315p093030	GI4_042019_J111315p0
IC0719	S0	29.4	A	42.73	48.45	0.35	0.43	50	AllWISE	AIS_232_sg80	AIS_232_sg80
IC0782	SBab	36.3	A	18.53	22.42	0.65	0.75	60	AllWISE	GI6_001033_GUVICS033	GI3_079021_NGC42
IC1024	S0	24.2	A	33.1	38.67	0.4	0.51	30	AllWISE	MISDR1_33738_0535	MISDR1_33738_05
IC1459	E1	29.0	R	97.03	100.97	0.84	0.86	40	AllWISE	GI1_093001_IC1459	GI1_093001_IC145
IC2006	E1	20.0	R	46.86	48.75	0.88	0.89	50	AllWISE	AIS_423_sg76	AIS_423_sg76
IC3370	E2 pec	27.0	R	66.94	69.65	0.85	0.87	55	AllWISE	–	–
IC3631	S0-a	42.0	A	24.4	28.31	0.6	0.7	90	AllWISE	GI6_001074_GUVICS074	AIS_223_sg22

Notes: Galaxy information and aperture photometry parameters. Columns: (1) galaxy name; (2) morphological type; (3) distance in Mpc; (4) Originating Sample (A: ATLAS^{3D} R: Rampazzo et al. (2013) B: Both); (5) W1 aperture semimajor axis in arcseconds; (6) W4 aperture semimajor axis in arcseconds; (7) W1 aperture axis ratio; (8) W4 aperture axis ratio; (9) Position Angle (10) *WISE* data release catalog; (11) *GALEX* NUV tilename; (12) *GALEX* FUV tilename. References for morphological type and distance come from Cappellari et al. (2011) and Rampazzo et al. (2013). The full version of this table with the full galaxy sample is included in the online journal article.

and otherwise used AllWISE. The data release of each image is included in Table 1.

We measured elliptical aperture photometry with the *ellipse* package in IRAF using the adjusted K20 parameters given in Table 1. Sky values were estimated via the *fitsky* package in IRAF. The inner radius of the annulus was chosen to be 1.5 times the semimajor axis of the photometric aperture in order to exclude galaxy flux. The thickness of the annulus was chosen to be 30 pixels in order to provide sufficient sky pixels to adequately measure the background.

We used SExtractor (Bertin & Arnouts 1996) to detect and mask foreground sources in the *WISE* W1 Atlas images, and then applied the masks to all four *WISE* bands. The most reliable method of foreground removal is PSF subtraction, as done in Jarrett et al. (2013). However, this method is not feasible for our large sample of galaxies due to the spatially variable PSF in the Atlas images. Since the stellar emission in ETGs is morphologically smooth, foreground stars bright enough to significantly affect the galaxy's flux are easily identified by SExtractor.

We also analyzed the 17 galaxies (including 3 ellipticals) from Jarrett et al. (2013) in order to test our pipeline. We excluded the M51 pair because none of our targets require similarly complex deblending. After comparing the flux measured from our pipeline to those reported by Jarrett et al. (2013), we encounter RMS differences of W1: 0.05 mag, W2: 0.06 mag, W3: 0.12 mag, and W4: 0.07 mag; we adopt these values as estimates of our photometric uncertainties. Since the Jarrett et al. (2013) sample is more morphologically complex than our measurements, we expect these differences are upper limits to the true photometric uncertainties. These differences cannot be explained by color corrections, which only correspond to 1% differences. Our measurements for the full sample are provided in Table 2, and have not been corrected for extinction. The uncertainties in Table 2 are formal uncertainties, and include zero-point uncertainties of 0.006, 0.007, 0.015, and 0.012 mag for W1, W2, W3, and W4, respectively. For our analysis, we apply extinction corrections for 2MASS and *WISE* bands from Indebetouw et al. (2005).

3.2 *GALEX*

The *GALEX* GR6/7 data release has images from six different observing programs with varying breadths and depths. The deepest is the targeted GII program, followed by several science surveys. The surveys vary in both sky coverage and exposure time, reaching 29,000 s for fields with well-studied galaxies, down to $\sim$ 100 s for the shallowest survey, which covers 63% of the sky. For galaxies observed in multiple surveys, we chose the highest exposure-time image which contained the entire photometric aperture in the field-of-view. Although the PSF is distorted near the edge of the field (Morrissey et al. 2007), we found that this did not affect the photometry. The tilename for each galaxy identifies the exposure and is given in Table 1.

We similarly used *ellipse* in IRAF to measure the *GALEX* images, although we estimated the sky differently. While the *GALEX* pipeline provides background images, we noticed galaxy flux in the background images for some objects. We therefore opted for traditional background estimation from an annulus. Unfortunately, *fitsky* in IRAF does not perform well when the background counts are very small, as it expects sky values to be normally distributed. We therefore implemented the method described in Gil de Paz et al. (2007), which divides two elliptical annuli into radial segments and averages over those segments. Similar to Gil de Paz et al. (2007), we divided the annuli into 90 segments total, with a typical segment area of 4000 pixels. We set the semimajor axis of the inner annulus at 1.5 times the semimajor axis of the photometric aperture. The uncertainty of the background comes from the standard deviation of the segment mean values.

We tested our approach with 20 morphologically diverse galaxies from the Gil de Paz et al. (2007) atlas which overlapped our sample, and used the same D25 aperture. Despite using the same technique, we systematically measured less flux than Gil de Paz et al. (2007) by 0.1 to 0.4 mag. We did successfully reproduce the Gil de Paz et al. (2007) results with the original cutouts from the NASA/IPAC Ex-

Table 2. Galaxy magnitudes for the ATLAS^{3D} and Rampazzo et al. (2013) samples.

Galaxy (1)	FUV (2)	σ_{FUV} (3)	NUV (4)	σ_{NUV} (5)	W1 (6)	σ_{W1} (7)	W2 (8)	σ_{W2} (9)	W3 (10)	σ_{W3} (11)	W4 (12)	σ_{W4} (13)
IC0560	21.49	0.117	19.40	0.035	13.27	0.006	13.93	0.009	14.35	0.056	13.67	0.154
IC0598	–	–	–	–	12.93	0.006	13.59	0.008	14.59	0.062	14.35	0.296
IC0676	18.11	0.054	16.92	0.031	12.46	0.006	13.01	0.008	11.06	0.016	9.681	0.013
IC0719	17.29	0.072	16.68	0.037	12.34	0.006	12.96	0.008	12.07	0.017	11.99	0.045
IC0782	21.57	0.108	19.21	0.035	13.93	0.007	14.62	0.012	15.78	0.142	>14.8	–
IC1024	17.31	0.052	16.77	0.031	12.60	0.006	13.04	0.007	11.02	0.015	10.29	0.013
IC1459	16.74	0.051	15.64	0.030	9.566	0.006	10.25	0.007	11.30	0.022	11.58	0.095
IC2006	18.47	0.109	17.14	0.041	11.25	0.006	11.93	0.007	13.26	0.037	13.67	0.226
IC3370	–	–	–	–	10.62	0.006	11.26	0.007	12.00	0.020	12.15	0.072
IC3631	17.61	0.078	16.87	0.030	13.98	0.007	14.63	0.012	15.39	0.180	>14.4	–

Notes: Calculated magnitudes for galaxies in our sample reported in the AB system. They have not been corrected for extinction. Columns: (1) Galaxy name; (2) FUV magnitude; (3) FUV magnitude uncertainty; (4) NUV magnitude; (5) NUV magnitude uncertainty; (6) W1 magnitude; (7) W1 magnitude uncertainty; (8) W2 magnitude; (9) W2 magnitude uncertainty; (10) W3 magnitude; (11) W3 magnitude uncertainty; (12) W4 magnitude; (13) W4 magnitude uncertainty. Uncertainties contain statistical and calibration uncertainties. All upper limits are 3σ upper limits. Blank UV entries mean that no *GALEX* observations were taken. The full version of this table with the full galaxy sample is included in the online journal article

tragalactic Database (NED)[6], so we conclude that the discrepancy is due to changes in the *GALEX* pipeline. We also compare our measurements with Bai et al. (2015), who remeasured the Gil de Paz et al. (2007) atlas using data processed by the current GR6/7 pipeline. Our results agree with Bai et al. (2015) to an RMS difference of 0.14 mag without a systematic trend in both the NUV and FUV bands, which we attribute to different background estimation methods. We conclude that our UV measurements are accurate and have an RMS precision of 0.14 mag.

Our *GALEX* measurements are also in Table 2. They have not been corrected for extinction, although for all of our analysis we used the prescription in Gil de Paz et al. (2007) to apply extinction corrections to these measurements. Values for E(B-V) are from the Schlegel et al. (1998) maps obtained from the IRSA dust map service.

3.3 Separating Dusty Galaxies

Fig. 2 shows a color-absolute magnitude diagram that illustrates the diversity in the shape of the SED for the ATLAS^{3D} and Rampazzo et al. (2013) galaxies. The majority of ETGs are extremely deficient in UV photons, as is expected from their generally old stellar populations. There appears to be a trend in the SED, where more UV-rich galaxies tend to be less luminous. This trend appears unrelated to the MIR classes of Rampazzo et al. (2013), although the RSA *Spitzer*-IRS atlas contains few low-luminosity ETGs. The region with blue ETGs is also sparely populated compared to the area with NUV-W1> 5. The Class-4 object which is an outlier at the bottom-right is NGC 1275, a Seyfert 1.5 galaxy in the Rampazzo et al. (2013) sample. There does not appear to be foreground contamination for this galaxy, so we believe the extreme NUV-W1 color and luminosity are due to the AGN component.

As indicated by Rampazzo et al. (2013), about half of ETGs contain observable traces of interstellar dust, which can dominate the MIR signal. We therefore attempted to separate the passive from the non-passive galaxies. For the Rampazzo et al. (2013) sample, non-passive galaxies are classified from *Spitzer*-IRS spectra as Class-1–4 fairly reliably. The ATLAS^{3D} sample does not have MIR spectra, so we attempt to distinguish between passive and non-passive galaxies with the extensive ancillary data.

Martini et al. (2013) demonstrated a one-to-one correspondence between optical dust lanes observed with the *Hubble Space Telescope (HST)* and emission from cold dust detected by *Spitzer* MIPS. We attempted to remove obvious contaminants with observed dust features in r-band observations (Krajnović et al. 2011). However, since the photometric resolution of SDSS is significantly lower than HST, we also searched for false negatives in our sample by cross-matching the dust detections in Martini et al. (2013) to the non-detections in Krajnović et al. (2011). This revealed many cases where the ATLAS^{3D} images did not reveal dust lanes that were clearly visible with HST and via FIR detections, so we also excluded galaxies with CO detections (Young et al. 2011).

Fig. 3 shows the W1-W3 vs. W1-W4 colors for galaxies without evidence for diffuse, interstellar dust. We also compare this sample to SPS tracks with metallicities that bracket the ATLAS^{3D} sample. We used SPS models with an exponential SFH timescale of 100 Myr. We also included a minimum sSFR of 10^{-14} yr^{-1} to account for constant, very low levels of star formation (Ford & Bregman 2013). Fig. 3 shows that the Flexible Stellar Population Synthesis (FSPS) high and median metallicity model tracks follow the shape of the data quite well, albeit with an offset. We explore the source of this offset in Section 4.2.

When compared to the passive Class-0 galaxies from Rampazzo et al. (2013), there still appears to be a tail extending redward of the clump of Class-0 galaxies. The single Class-0 object in the tail is NGC 4377, which has potential foreground contamination. Therefore, we performed an external check on this sample by cross-matching with *Herschel* detections at FIR wavelengths (Smith et al. 2012; di Serego Alighieri et al. 2013; Amblard et al. 2014). For objects in Amblard et al. (2014) we defined a "dust detection"

[6] https://ned.ipac.caltech.edu

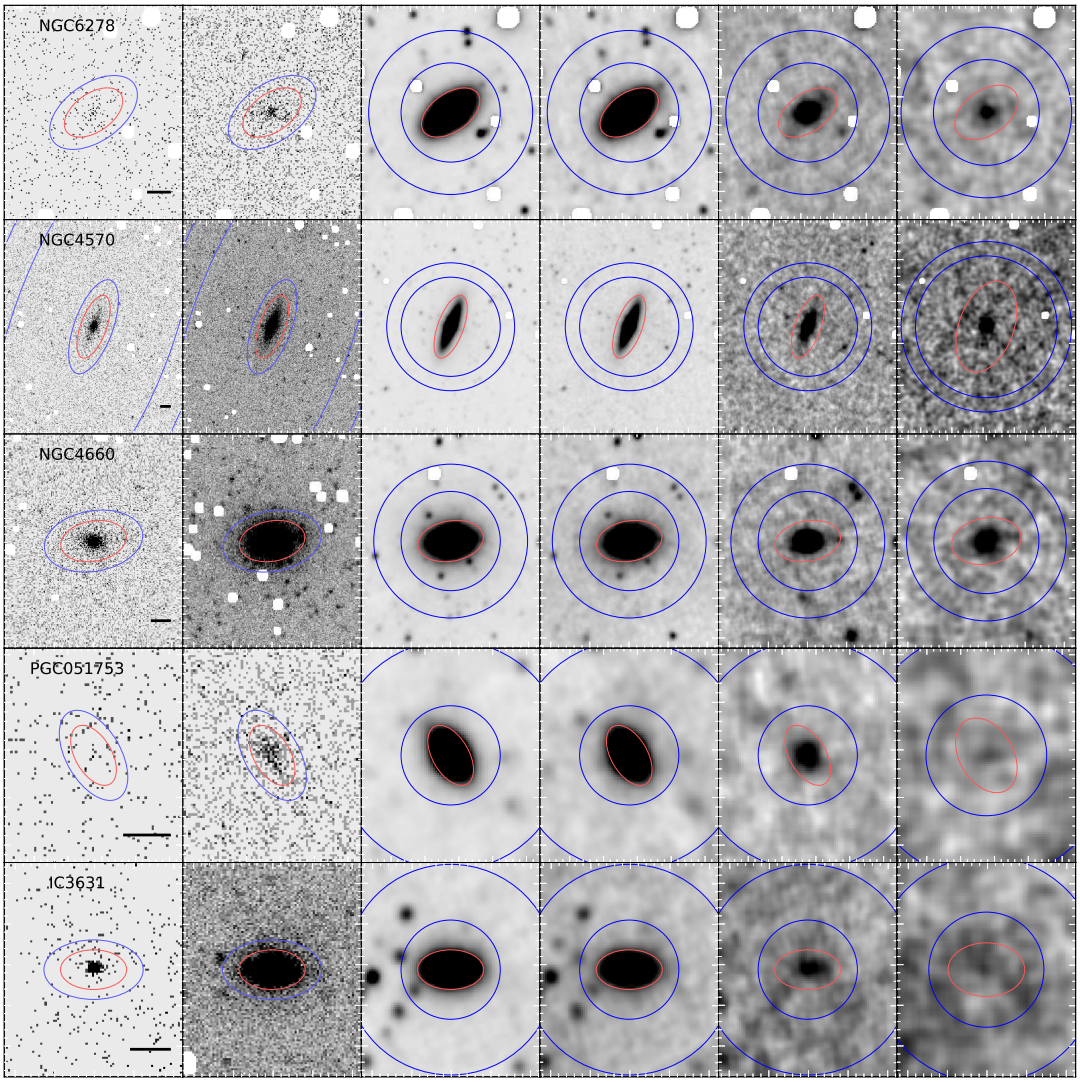

Figure 1. Cutouts of selected galaxies in *(Left to right:) GALEX* FUV and NUV, and *WISE* W1, W2, W3, and W4. The white regions are masked pixels, the photometric aperture is in red, and the sky annulus is in blue. Galaxies are shown in order of decreasing ATLAS^{3D} stellar mass from top to bottom. Scale is preserved from left to right, and a 30″ scalebar is shown in the bottom right of each FUV image. IC 3631 is not detected in W4. PGC 051753 is not detected in either FUV or W4.

as a 5σ detection in at least one of the 250 μm, 350 μm, and 500 μm bands. For galaxies from the other two studies, we used their internal criteria to indicate a dust detection. We note that two of the Class-0 objects had *Herschel* FIR detections, along with 31% of the overlapping ATLAS^{3D} sample, which suggests there is still substantial contamination. The region of the color-color diagram not populated by the galaxies with FIR detections is $W1 - W3 < 0.67$ and $W1 - W4 < 1.52$ (AB: $W1 - W3 < -1.85$ and $W1 - W4 < -2.40$). NGC 4486A, a tidally disrupted satellite of M87, is the only galaxy in this region with a marginal *Herschel* detection at 250 μm. Because of its tidal interactions, we classify it as a peculiar case, and assume that the rest of the galaxies in this region do not contain interestellar dust. We denote the galaxies in this region as the "color-cut dustless" sample, compared to the subset with only CO and/or dust exclusions, which we just term "dustless".

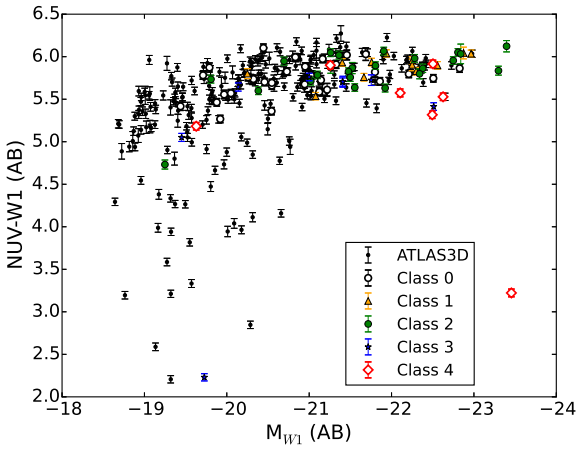

Figure 2. NUV-W1 vs W1 luminosity for the Rampazzo et al. (2013) and ATLAS^{3D} galaxies. These quantities are reasonable proxies for the shape of the radiation field and stellar mass, respectively. There is no clear trend between Rampazzo et al. (2013) class and NUV-W1, even for the Class-2 galaxies with anomalous PAH ratios. The luminous, blue Class-4 object is NGC 1275, which is a Seyfert 1.5 and thus may not be representative of ETGs.

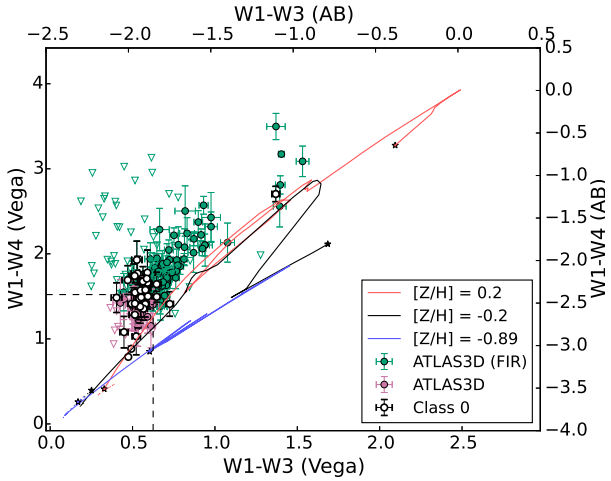

Figure 3. W1-W3 vs. W1-W4 colors of ATLAS^{3D} galaxies without CO or dust detections. Circles are data and triangles are upper limits due to W4 non-detections. The dashed black lines represent the "color-cut" criteria. Magenta and green points represent galaxies inside and outside the "color-cut" dustless region, respectively. Also shown is the passive Class-0 sample from Rampazzo et al. (2013). These data are compared to circumstellar tracks from Flexible Stellar Population Synthesis models. The red track corresponds to the highest metallicity galaxy in the ATLAS^{3D} sample with [Z/H]=0.2. The black track corresponds to the median metallicity in the ATLAS^{3D} sample of [Z/H]=-0.2. The blue track corresponds to the lowest metallicity galaxy with [Z/H]=-0.89. The beginning of the track at 1 Gyr is marked with a star, and continues until 14 Gyr. Solid tracks represent the FSPS model with the circumstellar dust model of Villaume et al. (2015); the very short dotted tracks in the lower left corner are the same models without circumstellar dust.

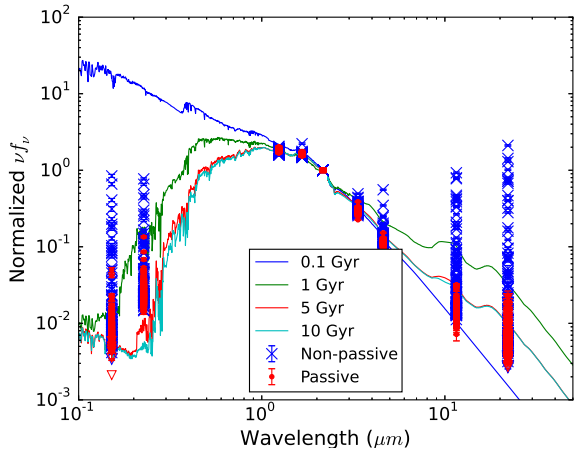

Figure 4. Spectral Energy Distributions of galaxies within the K20 aperture from broadband FUV, NUV, J, H, Ks, W1, W2, W3, W4 photometry, normalized to the K_s band. Model spectra are high-metallicity FSPS models (Conroy et al. 2009; Conroy & Gunn 2010) with exponentially decreasing SFH with τ_{SFH} = 100 Myr and [Z/H] = 0.2. The different spectra represent t=0.1, 1, 5, and 10 Gyr ages. Data points are the combined ATLAS^{3D} and Rampazzo et al. (2013) galaxies. ATLAS^{3D} galaxies without CO detections and dust lane morphology, or Rampazzo et al. (2013) Class-0 galaxies make up the passive group, while those with either detection, or classified as Rampazzo et al. (2013) Class-1–4, are in the non-passive group.

4 STELLAR POPULATION SYNTHESIS MODELS AND CIRCUMSTELLAR DUST

We used the *GALEX*, 2MASS, and *WISE* photometry to construct broadband SEDs for our sample. These SEDs are shown in Fig. 4, normalized to the K_s band. NGC 2974 is a very large outlier in W1 and W2, most likely due to very severe foreground contamination from a nearby bright star. While its photometry is reported in Table 2, we exclude it from our plots due to its suspect color.

We compare our data to the FSPS v2.5 models (Conroy et al. 2009; Conroy & Gunn 2010), which recently incorporated circumstellar dust (Villaume et al. 2015). These models allow for very extensive customization of isochrones and stellar atmosphere libraries. The FSPS models match the data well, particularly in the UV. In W3 and W4 many of the points extend above the model predictions. However, galaxies in the dustless sample described in Section 3.3 fall well within the range of colors predicted by the models.

4.1 Stellar Mass-to-Light Ratios

One valuable use for SPS models has been to predict stellar mass-to-light ratios (M/L) for galaxies from broadband colors (Bell & de Jong 2001; Bell et al. 2003; Zibetti et al. 2009). Bell & de Jong (2001) illustrated the power of this approach with their relation between M/L_B and $B-R$ color, which was largely robust to metallicity, extinction, and bursty star formation history (SFH). More recent improvements to M/L determinations include the use of multiple colors and models of dust extinction (Zibetti et al. 2009).

Yet despite these improvements, the presence of young stellar populations and internal extinction remains a major source of uncertainty for these models (Bell & de Jong 2001; MacArthur et al. 2004; Zibetti et al. 2009). These uncertainties are less severe at longer wavelengths, where the effects of young stellar populations and extinction on the mass-to-light ratio are diminished (Meidt et al. 2014). However, this reduction in uncertainty comes at a cost of increased uncertainties in modeling the Asymptotic Giant Branch (AGB) phase in the stellar models, which are especially poorly studied at low metallicity (Maraston et al. 2006). SPS models predict that the impact of AGB stars peak around 1 Gyr and decrease at greater ages (Melbourne et al. 2012), so should be less important for most ETGs.

Many different prescriptions exist to determine stellar masses of galaxies (e.g. Meidt et al. 2014; Cluver et al. 2014) that are either directly based on or calibrated from SPS models (Bruzual & Charlot 2003; Salim et al. 2007). However, the accuracy of these prescriptions is limited by the uncertainties associated with models for evolved stars, the dust geometry, IMF, and SFH.

Stellar mass-to-light ratios determined by dynamical means from ATLAS^{3D} are extremely valuable because they are not dependent on the same assumptions made by SPS models, such as an IMF. Results from ATLAS^{3D} indicate a tension between stellar masses generated from SPS models and from dynamics, which is correlated with observed velocity dispersions. This disagreement has been put forward as evidence that the IMF may be variable (van Dokkum & Conroy 2012; Cappellari et al. 2012), which would imply greater and systematic uncertainties in SPS-derived stellar masses that assume a universal IMF.

In order to determine if the tension is also seen in the MIR, we transformed the ATLAS^{3D} mass-to-light ratio from r-band to W1, and corrected for the difference between the largest Multi-Gaussian Expansion (MGE) aperture used in ATLAS^{3D} and the modified K20 aperture used here. The band was transformed according to the formula:

$$\log_{10}\left(\frac{M}{L_{W1}}\right)_{K20} = \log_{10}\left(\frac{M}{L_r}\right)_{MGE} + \log_{10}\left(\frac{L_r}{L_{r,\odot}}\right) + 0.4\left(m_{W1}|_{MGE} - 5\log_{10}\left(\frac{d}{10pc}\right) - M_{W1,\odot}\right) \quad (1)$$

where $(M/L_{W1})_{K20}$ is the mass-to-light ratio within the K20 aperture in W1, $(M/L_r)_{MGE}$ is the ATLAS^{3D} mass-to-light ratio within the region where the surface brightness is accurately modeled by the MGE, $L_r/L_{r,\odot}$ is the r-band luminosity of the galaxy in units of the in-band solar luminosity with $M_{r,\odot} = 4.64$ in AB magnitudes (Blanton & Roweis 2007), m_{W1} is the AB magnitude of the galaxy as measured in this work, d is the distance to the galaxy, and $M_{W1,\odot} = 5.94$ mag is the absolute magnitude of the Sun in AB magnitudes (transformed from the Vega value in Jarrett et al. (2013)). This transformation assumes that the stellar mass-to-light ratio is spatially constant, which is consistent with assumptions made in JAM modeling (Cappellari et al. 2013). In order to find an aperture representative of the total flux of the galaxy measured by ATLAS^{3D}, we numerically integrated the MGE intensity model in an elliptical aperture such that at least 90% of the flux would be in that aperture. This cutoff was chosen because the accuracy of the integrated flux of the MGE models compared to SDSS fluxes is 10% (Scott et al. 2013). The transformed mass-to-light ratios are shown in Fig. 5. The uncertainty of the mass-to-light ratio for each data point includes the photometric and zero-point uncertainties in W1, the photometric uncertainty in r-band (Scott et al. 2013), JAM modeling uncertainties (Cappellari et al. 2013), and distance uncertainties (Cappellari et al. 2011).

Although extinction is greatly reduced in the MIR, non-stellar emission—dust in particular—can be a major contaminant, introducing uncertainties of up to 30% when integrated over the entire galaxy (Meidt et al. 2012). We therefore use the color-cut dustless sample, described in Section 3.3, to minimize interstellar dust contamination.

The color-cut dustless galaxies in Fig. 5 do not appear affected by diffuse, interstellar dust, nor is there a noticeable trend in W1-W2. We calculate that $\log_{10} M/L_{W1} = 0.07 \pm 0.13$ for old stellar populations without diffuse dust. This value contrasts with the result of Meidt et al. (2014) of $\log_{10} M/L_{W1} = 0.25 \pm 0.11$. The offset is consistent with the IMF transition from Chabrier (2003) to Salpeter (1955) with increasing velocity dispersion found by Cappellari et al. (2012) and van Dokkum & Conroy (2012). To illustrate the continuum of IMFs, we include FSPS tracks along metallicities $[Z/H] = -0.89$, $[Z/H] = 0.0$, and $[Z/H] = 0.20$ which include the bounds of the ATLAS^{3D} sample and solar metallicity, with both Chabrier (2003) and Salpeter (1955) IMFs. The majority of objects, as well as the average M/L_{W1}, lie between these two bounds. This explanation fits our observations better than the Chabrier (2003) IMF assumed by Meidt et al. (2014).

The data may have a smaller range of W1-W2 than predicted by the FSPS models because the FSPS models do not include the metallicity-dependent CO absorption line in W2 (Peletier et al. 2012; Norris et al. 2014). We applied the GLIMPSE-calibrated correction described in Meidt et al. (2014) to the W1-W2 colors, which resulted in a narrower and slightly bluer range of W1-W2 than observed in the color-cut dustless sample.

One factor which may affect our interpretation of the M/L difference is that the color-cut used to separate dustless galaxies could preferentially select against galaxies with certain velocity dispersions if there is a trend with stellar populations. We found that the color-cut did preferentially select high velocity dispersion galaxies, so we fit a second time and only excluded galaxies with CO/dust detections. The new criteria sampled a broader range of velocity dispersion and resulted in a revised value of $\log M/L_{W1} = -0.03 \pm 0.17$. This is closer to the Meidt et al. (2014) value, but still discrepant at the 2σ level.

We also compare our results to an empirically-derived M/L ratio from GAMA using *WISE* colors (Cluver et al. 2014). This relation differs from that in Meidt et al. (2014) in two respects. First, the Meidt et al. (2014) relation was fit to a grid of Bruzual & Charlot (2003) models, rectilinear in age and metallicity. In contrast, the Cluver et al. (2014) relation was fit to the resolved portion of the GAMA sample, with stellar masses derived from optical colors (Taylor et al. 2011). This difference in how the fits are populated likely leads to the difference in the slope. Secondly, the Meidt et al. (2014) relation was fit to a pure stellar population, while the Cluver et al. (2014) relation was fit to very dusty galaxies.

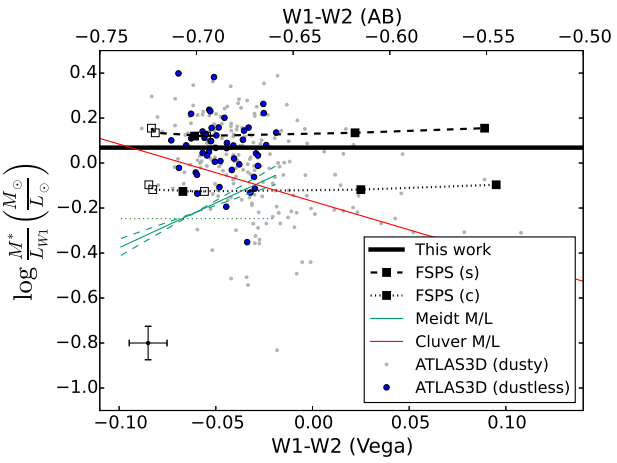

Figure 5. Stellar mass-to-light in the W1 band for the ATLAS^{3D} sample along with several SPS predictions and empirical measurements. The data points are converted from the ATLAS^{3D} r-band stellar mass-to-light ratio, corrected to match the 2MASS K20 aperture. Large blue points meet the color-cut dustless criteria defined in Section 3.3, while small grey points do not. A representative error bar is given in the lower left. The red line is the relation of Cluver et al. (2014) from the GAMA survey. The green solid and dashed lines indicate the M/L vs. W1-W2 relation and dispersion from Meidt et al. (2014) for old, stellar populations, derived from the Bruzual & Charlot (2003) models. The horizontal dotted green line represents the color-independent M/L suggested by Meidt et al. (2014) using an age-metallicity relation for ETGs. The dashed and dotted lines connect square points from FSPS models with Salpeter (1955) and Chabrier (2003) IMFs, respectively, evaluated at three different metallicities (from left to right): [Z/H] = -0.89, 0.0, 0.20 for a 10 Gyr population. Closed squares use W1-W2 directly from FSPS. Open squares use W1-W2 colors as corrected by Meidt et al. (2014).

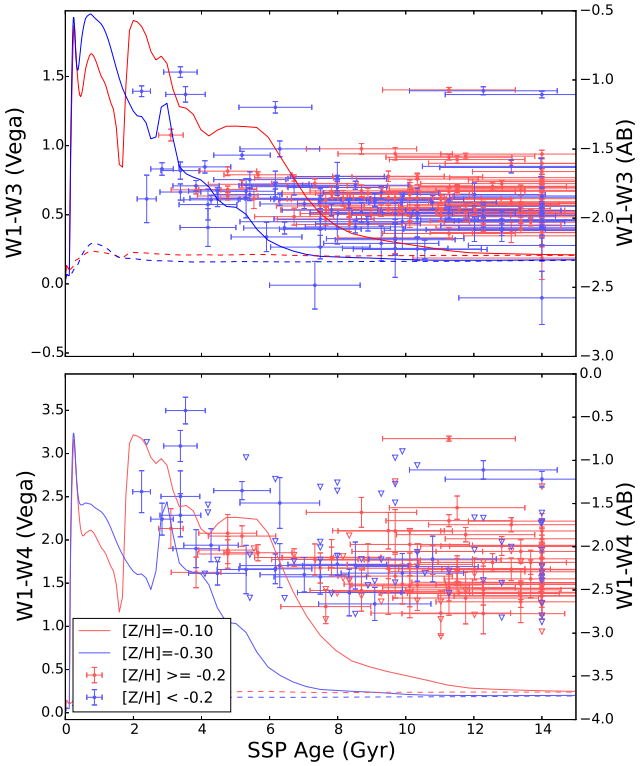

Figure 6. Colors of ATLAS^{3D} galaxies vs. SSP age compared with color evolution from FSPS for W1-W3 *(Top)* and W1-W4 *(Bottom)*. Red and blue lines represent SSP models 0.1 dex above and below the median metallicity of the ATLAS^{3D} sample, which should bound 60% of the ATLAS^{3D} sample in metallicity. The solid lines represent the color evolution of the FSPS model with the circumstellar dust prescription of Villaume et al. (2015), while the dashed lines represent the same population without circumstellar dust. The ATLAS^{3D} points are similarly color-coded and represent galaxies which lie above and below the median metallicity value of $[Z/H] = -0.2$. Galaxies with SSP ages greater than 14 Gyr are reset to 14 Gyr. For objects without a robust W4 detection, upper limits to the color are shown instead.

This likely explains why the relation seems to trace the dusty population, but is very discrepant with the dust-free ETGs.

4.2 Evidence for Ubiquitous Circumstellar Dust

All low- to intermediate-mass stars (between 0.5–8 $M_{\odot}$) pass through the Asymptotic Giant Branch (AGB) when undergoing hydrogen and helium shell burning (Marigo et al. 2008). These stars have extremely cool and tenuous atmospheres where dust grains condense and drive mass-loss (Salpeter 1974a,b; Goldreich & Scoville 1976; Bedijn 1987). As a result, we expect to observe this stage of stellar evolution in populations with ages ranging from 100 Myr to greater than the age of the Universe. However, SSP models indicate that the effects of circumstellar dust on integrated MIR flux peaks at 1 Gyr after star formation, and then decreases significantly by 10 Gyr (Villaume et al. 2015).

Circumstellar dust emission has been proposed as an age tracer of old stellar populations because broadband optical colors have an age-metallicity degeneracy (Bressan et al. 1998). Despite the lack of specific MIR age indicators for the *WISE* bands, SPS modeling can potentially yield an evolutionary track for a given color due to circumstellar dust (Villaume et al. 2015). Bregman et al. (2006) showed that there is some tension between ages determined from optical line indices and circumstellar dust fits. We compare these two age determinations for the ATLAS^{3D} sample using the FSPS models. We also investigate the effect of circumstellar dust on star formation rate indicators in the MIR for galaxies with low specific SFRs (sSFR = SFR / M_*).

We used MIR colors to obtain a distance-independent measurement of circumstellar dust. Flux in the short-wavelength W1 and W2 bands is largely dominated by the stellar continuum and is not sensitive to dust (e.g. Villaume et al. 2015). In contrast, the longer-wavelength W3 and W4 bands should be increasingly sensitive to dust, since they lie in the region of the spectrum where circumstellar dust emission dominates over photospheric emission. We avoid the W2 band in comparing data to models because the effect of CO absorption alluded to in Section 4.1 has not been included in all SPS models (Peletier et al. 2012; Norris et al. 2014).

It is apparent from Fig. 3 that circumstellar dust is necessary in order to explain MIR colors; however, there is an offset between the tracks and the data. We explore the source of this offset in more detail in Figs. 6 and 7. In Fig. 6 we used SSP ages for the ATLAS^{3D} sample from McDermid et al.

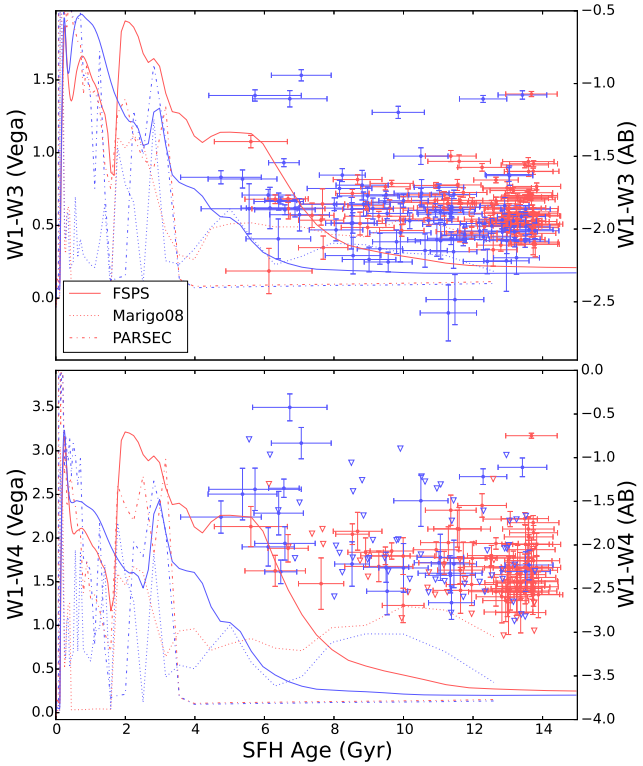

Figure 7. Comparison between models and data similar to Fig. 6, except with SFH ages instead of SSP ages. Red and blue colors have the same meaning as in Fig. 6. Line styles correspond to different SPS models: solid lines correspond to FSPS models, dotted lines correspond to Marigo et al. (2008) SSP models, and dot-dashed lines correspond to the PARSEC SSP models.

(2015) derived by fitting optical line indices. Since the SSP ages in McDermid et al. (2015) were not constrained to be consistent with the age of the Universe, we set the galaxies with SSP ages greater than 14 Gyr to have ages of 14 Gyr, in order to be consistent with current cosmological models (Planck Collaboration 2014); this was 19% of the sample. While the discrepancies in W1-W3 do not seem be too large, the models appear to underpredict the flux in W4 by a factor of 2.5, which is comparable to the offset seen in Fig. 3. As seen in Fig. 7, mass-weighted ages estimate galaxies to be older, making the offset even more apparent. The potential causes of this discrepancy could include a ubiquitous intermediate-age population whose influence is seen in the MIR, but not detectable in the optical, and that a wider mass range of AGB stars produce circumstellar dust at subsolar metallicities than predicted by the models.

Fig. 7 compares the FSPS models to the PARSEC v1.2S + COLIBRI PR16 SSP models (Bressan et al. 2012; Marigo et al. 2013; Rosenfield et al. 2016) and the Marigo et al. (2008) models. The PARSEC models seem to predict no circumstellar dust at late ages, exacerbating the tension seen with the FSPS models. On the other hand, the Marigo et al. (2008) models predict more dust at late times compared to both the FSPS and PARSEC models. However, the predicted colors of the dusty stellar population are still bluer than indicated by the data.

While some of the extremely red galaxies are likely contaminated by interstellar dust, it is significant that very few galaxies are consistent with having no circumstellar dust. Since the number of galaxies redder than the no-circumstellar-dust models is significantly greater than our estimated contamination rate, we conclude that circumstellar dust is the source of the MIR excess for galaxies without interstellar dust. These results are robust to differences in the IMF.

4.3 Impact of Circumstellar Dust on MIR SFRs

Accurate Star Formation Rates (SFRs) provide valuable insights into galaxy formation. The most direct method to determine SFR measures Balmer emission from HII regions, which is related to the number of ionizing photons from young stars; however, the extinction corrections can be substantial and uncertain (Kennicutt 1998b). SFRs derived from MIR to FIR observations are more indirect as they measure the SFR through radiation reprocessed by dust grains. This method is quite insensitive to extinction uncertainties, but at low SFRs the old stellar population may also significantly heat the dust (Helou 1986; Lonsdale Persson & Helou 1987; Kennicutt 1998a; Groves et al. 2012).

We quantify the important contribution of circumstellar dust to the total MIR luminosity, and its impact on SFR estimates with *WISE* W1, W3 and W4. W1 traces the old stellar population that dominates stellar mass, and W3 and W4 trace the PAHs and warm dust heated by young stars, respectively, so sSFR can be calculated without additional observations. Although W4 is considered a superior tracer of SFR over W3, fainter galaxies are more readily detected in W3. Since SFRs can be measured in W3 for galaxies too faint for a W4 detection, we include it in our analysis of SFR measurements.

Davis et al. (2014) investigated the impact of circumstellar dust on SFR for the ATLAS^{3D} sample using *WISE* catalog photometry, with prescriptions calibrated for *Spitzer* bands. We reinvestigate this prescription with our updated photometry, more stringent criteria for dustless galaxies, and with the more recent SFR relations of Cluver et al. (2014).

We plot the W1 vs. W3 and W4 luminosity for the ATLAS^{3D} sample in Fig. 8 (see Figure 1 of Davis et al. (2014) for a similar plot with K_s). The color-cut dustless sample described in Section 3.3 is shown in red. The color-cut sample was chosen because it should have less interstellar dust contamination compared to the regular dustless sample, and should represent an accurate relation between W1 and W3 (or W4) in the absence of star formation. Because we may have excluded some truly dust-free galaxies whose colors do not match our exclusion criteria, the scatter in our relation may be underestimated. Follow-up observations of the ATLAS^{3D} sample with FIR/submillimeter measurements or high-resolution visible-wavelength images to search for dust lanes would result in a more representative sample of dustless galaxies.

In order to characterize the minimum SFR which can be usefully measured with W4 observations, we calculate sSFR limits with the relations in Cluver et al. (2014) and use the mean W1-W2 value of our sample to get M/L_{W1}. The results shown in Fig. 8 indicate that the contribution of circumstellar dust to W3 and W4 will mimic an sSFR

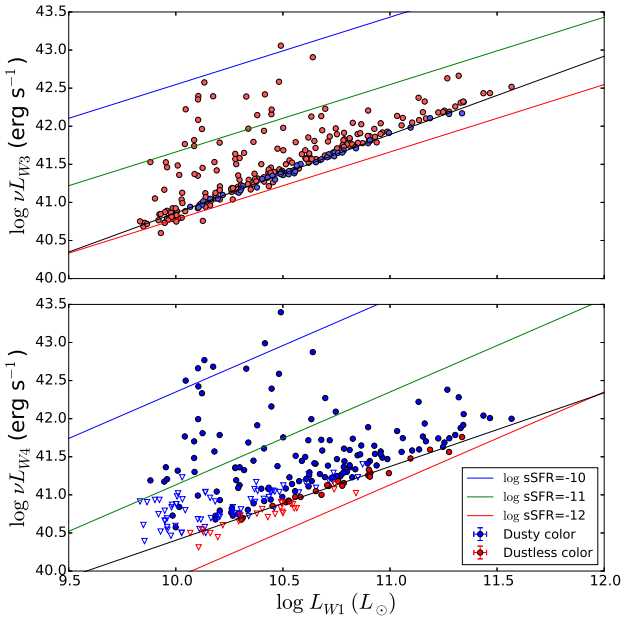

Figure 8. *(Top)* W3 vs. W1 and *(Bottom)* W4 vs. W1 luminosities for the ATLAS^{3D} sample. Circles are detections and triangles are W4 upper limits. Red points are in the dustless color-cut sample. Error bars are smaller than the points. The blue, green, and red lines represent where specific star formation rate is 10^{-10} yr^{-1}, 10^{-11} yr^{-1}, 10^{-12} yr^{-1}. The black line represents a fit to the color-cut dustless galaxy detections. Note that W3 is significantly more sensitive than W4.

of 2×10^{-12} yr^{-1}. Lower values of sSFR cannot be reliably inferred with integrated *WISE* photometry alone.

Even at larger sSFR values, it is still necessary to remove the effect of circumstellar dust. In order to quantify the effect, we fit a line to the dustless detections and obtain:

$$\log \nu L_{W3} = 1.03 \log L_{W1} + 30.58, \quad (2)$$

$$\log \nu L_{W4} = 0.97 \log L_{W1} + 30.72 \quad (3)$$

with an RMS scatter of 0.03 and 0.04 dex, where L_{W1} is the "in-band" luminosity in solar luminosities, and νL_ν is the spectral luminosity of the band in erg s^{-1}. These relations may be used to subtract the circumstellar dust contribution to W3 or W4 for relatively quiescent galaxies. The W4 relation is similar to the relation derived by Davis et al. (2014) between Ks and W4. These corrections will likely be negligible for typical star-forming galaxies as the sSFR of local L^* galaxies is around 10^{-10} yr^{-1} (Cluver et al. 2014).

5 PAH RATIOS WITH *GALEX* AND *WISE*

Mid-infrared spectra of early-type galaxies have shown that many exhibit much weaker short-wavelength PAH features (6.2, 7.7, and 8.6 μm) relative to those at longer wavelengths (e.g. 11.3 and 12.7 μm) (Kaneda et al. 2005, 2008; Vega et al. 2010; Rampazzo et al. 2013) compared to star forming galaxies (Helou et al. 2000; Brandl et al. 2004; Smith et al. 2007). Observations of later-type galaxies have also shown that low values of these band ratios are commonly found in low-luminosity AGN (Smith et al. 2007; O'Dowd et al. 2009). Many early-type galaxies contain evidence for LINERs (Ho et al. 1997), although as most may not be dominated by AGN (Sarzi et al. 2010), it is not clear if there is a direct connection between AGN and the proportionally weaker short-wavelength PAH bands in early-type galaxies.

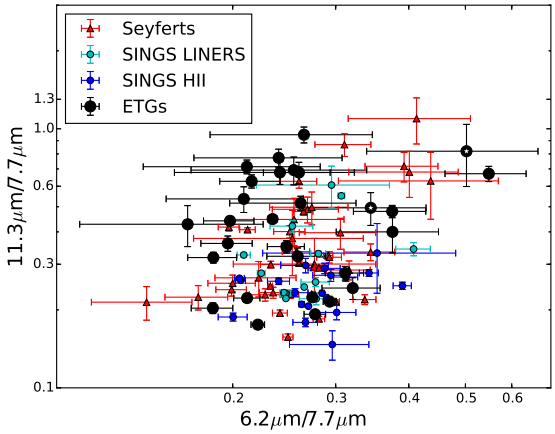

Figure 9. Plot of 11.3 μm/7.7 μm vs. 6.2 μm/7.7 μm line ratios for different samples of galaxies. Seyfert line ratios were taken from Diamond-Stanic & Rieke (2010); SINGS ratios were from Smith et al. (2007); the ETG sample contains galaxies from Smith et al. (2007) and Rampazzo et al. (2013). Stars indicate that the ETG is Class-4 according to Rampazzo et al. (2013).

5.1 Environments of Anomalous PAH Ratios

We have used data from three significant studies of PAH emission from nearby galaxies to probe the relationship between PAH emission, AGN, and host galaxy morphology to further explore the different PAH band ratios seen in early-type galaxies. The largest study of early-type galaxies is the RSA *Spitzer*-IRS Atlas by Rampazzo et al. (2013), and about half of their sample of ETGs exhibit PAH emission. Smith et al. (2007) performed a detailed analysis of PAH emission from galaxies in the *Spitzer* Infrared Nearby Galaxy Survey (SINGS: Kennicutt et al. 2003). This sample spans a wide range of luminosity and infrared to visible wavelength flux ratio, and includes early and late-type galaxies. They have also classified the galaxies as either "HII" galaxies, which are dominated by star formation, LINERs, or Seyferts. Finally, Diamond-Stanic & Rieke (2010) studied 35 Seyfert galaxies in the Revised Shapley-Ames catalog. All of these Seyferts have late-type host galaxies (later than S0), and generally exhibit weaker short-wavelength PAH emission compared to HII galaxies. This study included 21 galaxies with PAH emission in spectra not centered on the nuclear region, and these off-nuclear spectra exhibit PAH ratios similar to HII galaxies.

Diamond-Stanic & Rieke (2010) investigated if the weaker 6.2, 7.7, and 8.6 μm bands in Seyferts could be due to radiative or mechanical processing. Previous work (Szczepanski & Vala 1993; Hudgins & Allamandola 1995; DeFrees et al. 1993; Langhoff 1996) has shown that the $C-C$ stretching modes that give rise to the 6.2 and 7.7 μm

features, and the $C-H$ in-plane bending modes that give rise to the 8.6 μm feature, are more readily produced in ionized PAHs. The ratio of these features to the $C-H$ out-of-plane bending mode that gives rise to the 11.3 μm feature (Duley & Williams 1981; Allamandola et al. 1989) will be lower for more neutral PAHs. Fig. 9 shows the ratio of 11.3 μm/7.7 μm vs. 6.2 μm/7.7 μm for measurements from these three studies. The early-type galaxies include both the Rampazzo et al. (2013) sample and early-type galaxies in Smith et al. (2007), the Seyfert sample includes late-type Seyferts from both Smith et al. (2007) and Diamond-Stanic & Rieke (2010), and the LINERs and HII galaxies are only galaxies with late-type morphology from Smith et al. (2007). This diagram clearly shows that the early-type galaxies have larger 11.3 μm/7.7 μm than the HII galaxies, but also that the ratio is larger than for the Seyferts and perhaps the LINER sample. Only galaxies with detections in both ratios are shown, as the literature sources generally do not quote upper limits for non-detections. Very different values of 11.3 μm/7.7 μm vs. 6.2 μm/7.7 μm are expected for neutral vs. ionized PAHs. Allamandola et al. (1999) and Draine & Li (2001) showed that neutral PAHs lead to the intensity ratio 11.3 μm/7.7 μm > 0.4, whereas 11.3 μm/7.7 μm < 0.2 is more characteristic of ionized PAHs, although the value of this ratio also depends on the PAH size distribution, as does the 6.2 μm/7.7 μm ratio. Only about half of the ETGs have 11.3 μm/7.7 μm > 0.4 as expected for neutral PAHs.

Fig. 10 plots the cumulative distribution functions of these four classes of galaxies. We used a Kolmogorov-Smirnov two-sample test to measure the significance of the differences. We found that the 7.7 μm/11.3 μm difference between the early-type galaxies and the Seyferts, as well as between the early-type galaxies and the HII galaxies, is very significant ($p \ll 0.01$). The difference between the early-type galaxies and LINERs is marginally significant ($p \sim 0.02$) as well. Note that the LINER sample is somewhat smaller than the other samples, and that the cumulative distributions contain all galaxies with detections in the single ratio, and thus may have more points than Fig. 9.

Galliano et al. (2008) noted that the typical ionization state of PAHs is set by $G_0 T^{1/2}/n_e$ (Bakes & Tielens 1994), where G_0 is the intensity of the UV radiation field, T is the gas temperature, and n_e is the electron density, and we investigated if the distribution of Class-2 and Class-3 objects followed trends in any of these physical quantities. The gas temperature can be determined from the $H_2S(3)/H_2S(1)$ line ratio, and the electron density can be determined from [S III] 18.7 μm/[S III] 33.5 μm. These lines have been measured by Rampazzo et al. (2013), and any trends should cause the two classes to separate in one of the dimensions. As seen in Fig. 11, Class-2 and Class-3 objects have similar values of these ratios, so we conclude that trends with gas temperature or electron density are not the origin of the difference between the two classes.

Since the temperatures and densities for the Class-2 and Class-3 galaxies are similar, we expect the degree of ionization for PAHs will depend on the shape of the interstellar radiation field (ISRF) (Weingartner & Draine 2001). The ISRF in early and late-type galaxies varies dramatically, both in normalization and shape. The dramatic lack of young stars, and therefore UV emission, can even lead optical photons to become the primary heating mechanism for interstellar dust (Groves et al. 2012). While we do not directly measure the intensity of the ISRF, we use the NUV-J color as a proxy for the slope. We show the trend in the slope of the radiation field with the 7.7 μm/11.3 μm ratio in Fig. 12. Even though Class-4 objects also have PAH emission, they were excluded as likely AGN because their high 1.4 GHz and nuclear X-ray emission may distort the ISRF (Rampazzo et al. 2013). There does not appear to be any correlation between the shape of the ISRF and the 7.7 μm/11.3 μm ratio, which corresponds directly with MIR class.

While the relation between ionization state and UV intensity works well for many environments (Joblin et al. 1996; Bregman & Temi 2005), Diamond-Stanic & Rieke (2010) pointed out that many Seyferts have ratios consistent with completely neutral PAHs, or even more extreme ratios than the models allow, and in any case the more intense radiation field associated with AGN should not lead to less ionization. We find that the early-type galaxies often have even smaller values of the 7.7 μm/11.3 μm band ratio than the Seyferts. Draine & Li (2001) noted that smaller values of 7.7 μm/11.3 μm could be produced in the charging conditions characteristic of the Cold Neutral Medium (CNM) or Warm Ionized Medium (WIM), which have lower densities and radiation field intensities than typical of the Photodissociation Regions (PDRs) associated with star formation. If most of the PAHs are associated with conditions more similar to the CNM or WIM, this could explain the dramatic difference in their ratios relative to star-forming galaxies, as well as why they are not similar to Seyferts, which typically also have PDRs.

As the three shorter-wavelength PAH features are also associated with smaller PAHs, an alternative explanation of their proportionally lower fluxes is a different size distribution (Schutte et al. 1993; Draine & Li 2001; Galliano et al. 2008). Experimental work on PAHs has indicated that PAHs below 15-20 C atoms would be destroyed in most environments, PAHs smaller than 20-30 C atoms may be stripped of their H atoms, and PAHs of 30-50 C atoms would mostly be photoionized (Jochims et al. 1994; Allain et al. 1996). If smaller PAHs have been destroyed, then this would also lead to lower 6.2 μm relative to 7.7 μm and lower 7.7 μm relative to 8.6 μm. Fig. 13 shows these two ratios for the same galaxies shown in Fig. 9. Based on inspection of this figure, as well as Kolmogorov-Smirnov (KS) tests applied to the cumulative distributions, we do not see significant differences between the early-type galaxies and other populations. Diamond-Stanic & Rieke (2010) similarly did not find significant differences between Seyferts and either their off-nuclear positions or the HII galaxies from Smith et al. (2007). As illustrated in Draine & Li (2001), larger PAHs can also contribute to the larger 11.3 μm/7.7 μm ratios seen in Fig. 9, although they also have smaller 6.2 μm/7.7 μm ratios. Intriguingly, about half of the early-type galaxies have 6.2 μm/7.7 μm < 0.25, although the difference is not formally significant. Careful estimates of upper limits on the weak 6.2 μm feature in the several early-type galaxies with only 7.7 μm detections, as well as more sensitive measurements with future facilities, would help to better characterize the smaller PAHs in these galaxies that are most sensitive to destruction processes.

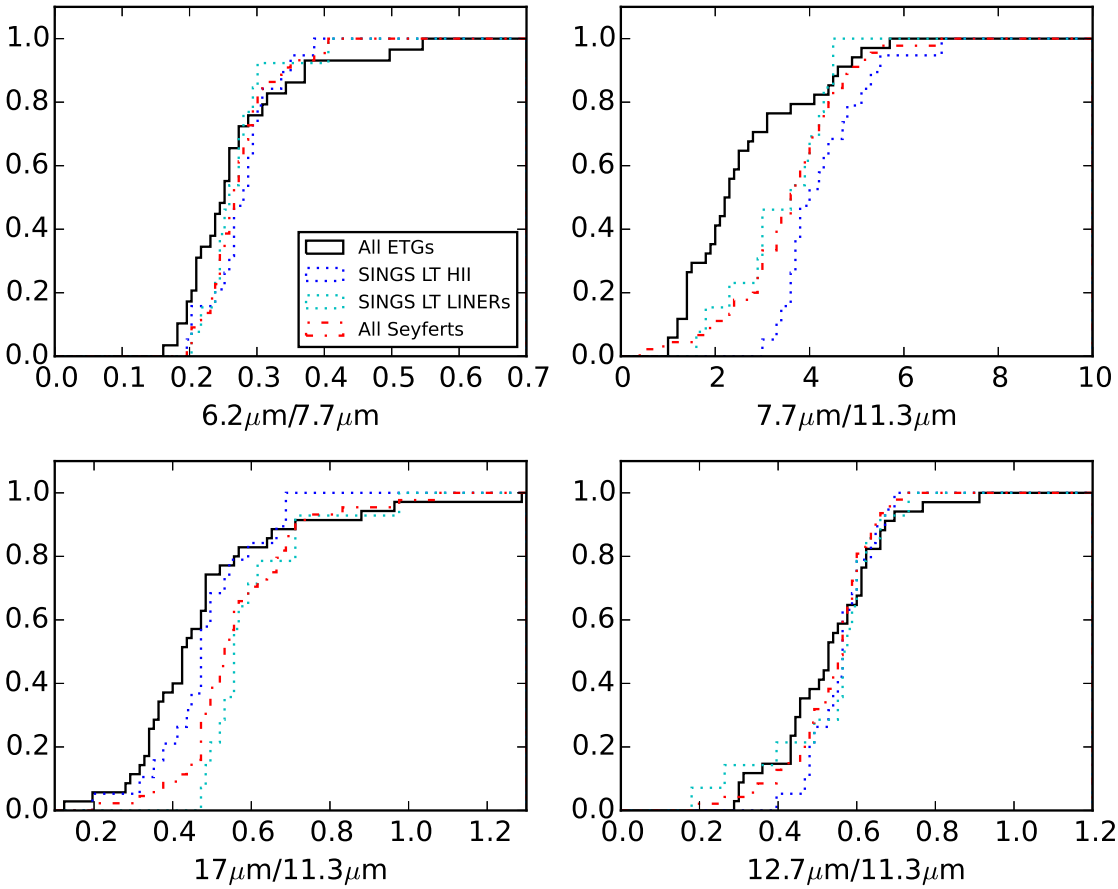

Figure 10. Cumulative distribution functions of the galaxy classes in Fig. 9 for *(Top left)* 6.2 μm/7.7 μm, *(Top right)* 7.7 μm/11.3 μm, *(Bottom right)* 12.7 μm/11.3 μm, *(Bottom left)* 17 μm/11.3 μm. There is a statistically significant difference between the ETGs and SINGS late-type (LT) HII galaxies, as well as the ETGs and Seyferts in 7.7 μm/11.3 μm. The distribution between ETGs and LINERs in 7.7 μm/11.3 μm was marginally significant. ETGs are also significantly different from Seyferts and LINERs in 17 μm/11.3 μm, but are similar to HII galaxies. There are no significant differences between the galaxy distributions in any of the other line ratios.

Another explanation proposed for the variations in 7.7 μm/11.3 μm is interstellar shocks. Shock velocities of on order 100 km s^{-1} can reduce the relative number of small grains (Jones et al. 1994; Micelotta et al. 2010), and thus lead to weaker emission in all three of the shorter-wavelength features. If shocks are present, then the galaxies may also exhibit strong H_2 emission. Many studies have found a correlation between H_2 emission and the 7.7 μm/11.3 μm ratio (Roussel et al. 2007; Ogle et al. 2007; Kaneda et al. 2008; Vega et al. 2010). Fig. 14 *(left)* illustrates the correlation shown by Diamond-Stanic & Rieke (2010) for the RSA Seyferts, along with the early-type galaxies from Rampazzo et al. (2013). The early-type galaxies mostly follow the same trend as the Seyferts, although they generally have more H_2 emission and there is more dispersion in 7.7 μm/11.3 μm for the early-type galaxies with the proportionally strongest H_2 emission. Diamond-Stanic & Rieke (2010) and Rampazzo et al. (2013) found that AGN power did not correlate with this ratio, and Fig. 14 *(right)* confirms this point with a plot of the ratio of $H_2S(3)/(7.7\ \mu m + 11.3\ \mu m)$ vs. nuclear X-ray luminosity from Pellegrini (2010). Processing by shocks appears to be a more viable contributor to the 7.7 μm/11.3 μm ratios in early-type galaxies, as it is for Seyferts.

In addition to the preferential destruction of small PAHs, shocks could also affect the chemistry of the PAHs, even those that are fully hydrogenated. For example, the 11.3 μm band is produced by single C—H bonds, while the 12.7 μm feature is produced by C—H multiplets (Hony et al. 2001). Diamond-Stanic & Rieke (2010) found that Seyferts exhibit significantly smaller ratios of 12.7 μm/11.3 μm than off-nuclear and HII galaxies, which could be due to different processing. Figs. 10 and 15 shows that the early-type galaxies are not significantly different from the Seyferts or the HII galaxies, so we see no evidence that this is an important physical difference in the early-type galaxy population.

The 12.7 μm/11.3 μm band ratio shown in Fig. 15 is plotted vs. the 17 μm/11.3 μm band ratio. Both the 11.3 μm band and the 17 μm band originate from neutral

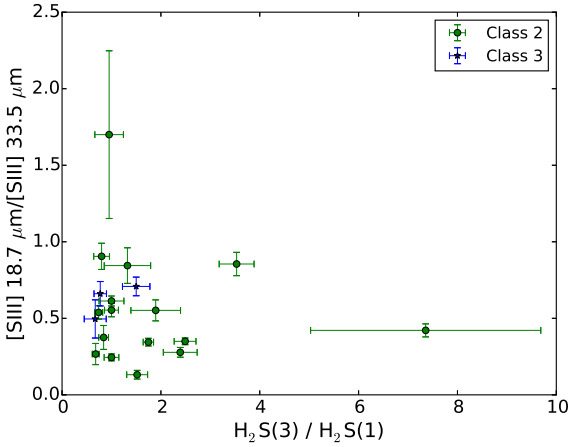

Figure 11. Class-2 and Class-3 sulfur and molecular hydrogen line ratios as measured in Rampazzo et al. (2013). We expect $H_2S(3)/H_2S(1)$ to be a proxy for the gas temperature of the emitting region, and [S III] 18.7 μm/[S III] 33.5 μm to be a proxy for the electron density. Objects without detections in any of the lines have been excluded from the figure. There does not appear to be a significant distinction between these two classes in this plane.

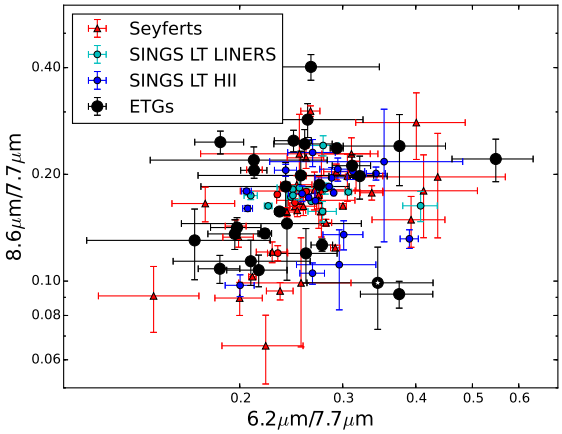

Figure 13. Plot of line ratios like Fig. 9 except for 8.6 μm/7.7 μm and 6.2 μm/7.7 μm line ratios. Larger grain size distributions tend to have suppressed 6.2 μm/7.7 μm emission. There are no statistically significant differences in the ratios between classes, indicating that a systematic difference in grain size distribution may not be correlated with anomalous PAH emission.

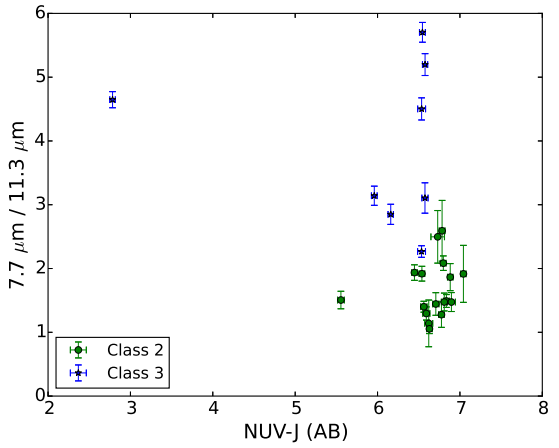

Figure 12. Distribution of Class-2 and Class-3 sources in NUV-J, which acts as a proxy for the slope of the ISRF, and 7.7 μm/11.3 μm, which reflects the level of "anomaly" in the PAH ratios.

PAHs, and so their relative strength is primarily sensitive to the size distribution. Smith et al. (2007) found that larger 17 μm/11.3 μm intensity ratio correlates with metallicity, and suggest that it may be easier to form the larger grains that contribute to the 17 μm band in higher metallicity environments. They find that 17 μm/11.3 μm is largest in Seyferts and suggest that these high ratios are due to a combination of the higher metallicities of the Seyfert hosts and the relative destruction of the carriers of the shorter wavelength 11.3 μm feature. As shown in Fig. 15, we find that early-type galaxies have significantly *lower* 17 μm/11.3 μm ratios than the Seyferts (KS $p < 0.0001$) and LINERs (KS $p < 0.0001$) from Smith et al. (2007), and are similar to HII galaxies (see also Fig. 10). Early-type galaxies may have lower 17 μm/11.3 μm band ratios because they lack the hard radiation field of Seyferts. Alternatively, this ratio could be lower in some early-type galaxies because their PAHs have been externally accreted from lower-metallicity dwarf galaxies.

We cannot separate the effect of metallicity on the 17 μm/11.3 μm ratio because of the sparse overlap between the ATLAS^{3D} and Rampazzo et al. (2013) samples. Only 13 galaxies in our sample have both ATLAS^{3D} metallicity and 17 μm/11.3 μm measurements; their Pearson correlation coefficient is -0.04, which indicates a very weak anticorrelation.

5.2 Photometric PAH classification

Currently the only way to discriminate between MIR classes is through infrared spectra from targeted spectroscopic observations in space. This is a significant investment for space-based missions which are already highly oversubscribed. Now that the *WISE* mission has imaged the entire sky in the MIR, a successful method of classifying galaxies into different MIR classes based on *WISE* data would allow demographic analysis of anomalous PAH emission.

Because most of the PAH emission features lie in the very broad W3 filter, we expect most of the discriminating power to occur with the W2-W3 and W3-W4 colors. We plot the Rampazzo et al. (2013) sample in Fig. 16. Many of the Class-4 objects lie far away from the bulk of the distribution, likely due to the hot dust continuum in their spectra. There also seems to be good discrimination between Class-0 and Class-2/3 objects in W2-W3. The Class-0 objects are systematically bluer than both the Class-2 (K-S $p < 10^{-4}$) and Class-3 (K-S $p < 10^{-6}$) objects. A cumulative histogram of both classes in W2-W3 is shown in Fig. 17. 85% of Class-0, 11% of Class-2, and no Class-3 objects are bluer than $W2 - W3 = 0.635$ (Vega, or -1.2 AB), providing a convenient color-cut between dusty and passive ETGs. No other

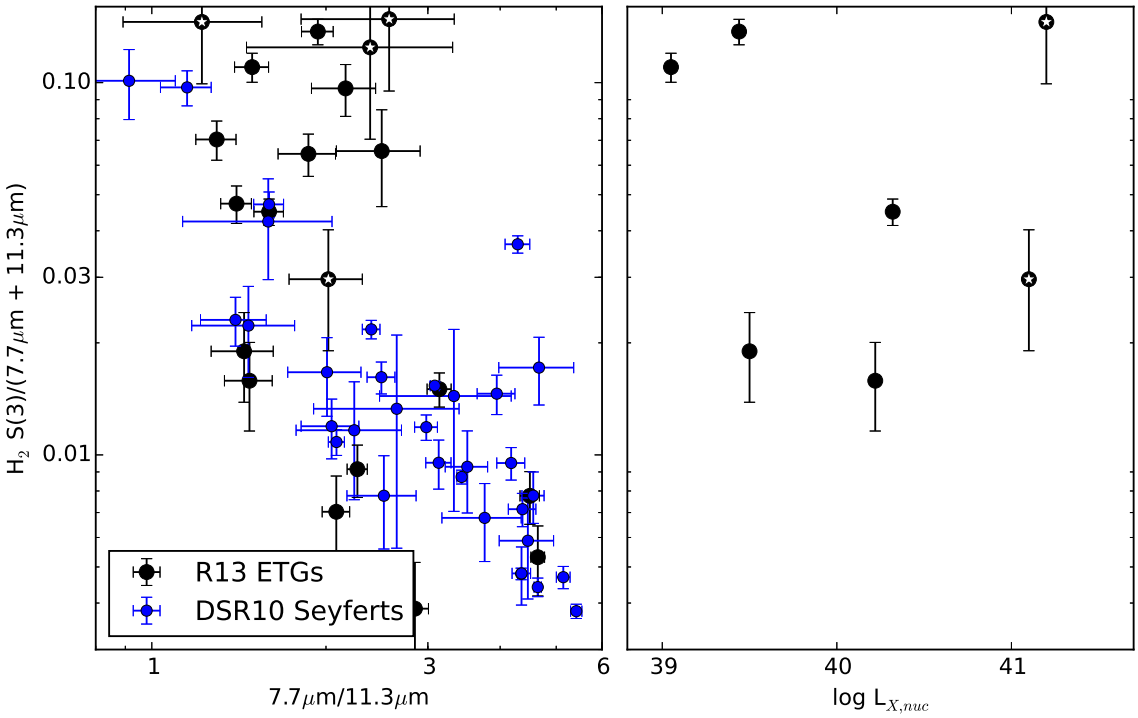

Figure 14. *Left:* Relative strength of the $H_2S(3)$ transition to PAH emission, which traces shocks in cold gas, versus the 7.7 μm/11.3 μm ratio. Black points are ETGs from Rampazzo et al. (2013) while blue points are Seyferts from Diamond-Stanic & Rieke (2010). Stars indicate Class-4 galaxies. Both the ETGs and Seyferts indicate a correlation between the shocks and anomalous PAH ratios. *Right:* Molecular hydrogen strength vs. nuclear X-ray luminosity for Rampazzo et al. (2013) galaxies with nuclear X-ray detections. As noted in Diamond-Stanic & Rieke (2010), there does not appear to be a trend between shock strength and X-ray luminosity.

major distinctions between classes are statistically significant.

One reason why *WISE* is unable to discriminate between classes very well is because the bands are not well-placed with respect to PAH features. The only band sensitive to PAH emission is W3, which covers all of the 7.7 μm, 8.6 μm, 11.3 μm, and 12.7 μm PAH complexes (Wright et al. 2010). The W3 band accomplishes this amount of spectral coverage with a wide effective bandwidth of 5.5 μm (Jarrett et al. 2011). By comparison, the typical equivalent width of a line is around 0.1 μm (Rampazzo et al. 2013). Therefore, the difference between the presence and absence of all five PAH lines is around 0.1 mag, which is similar to the photometric error of our measurements. While this should suffice to separate Class-0 objects from Class-2/3 objects, separation of Class-2 and Class-3 objects requires more precise photometry. Another complication is the large intrinsic scatter in Class-2 and Class-3, which we attribute to varying levels of contribution by the dust continuum.

Despite the fact that *WISE* colors on their own cannot discriminate between the MIR classes, they can be useful for informing follow-up targets. This will be particularly true with the Mid-Infrared Instrument (MIRI) on the *James Webb Space Telescope (JWST)*. For galaxies which have W2-W3 colors consistent with some interstellar dust, better demographics on the prevalence of anomalous PAH ratios can be determined from follow-up with the MIRI Medium Resolution Spectrograph (MRS).

6 CONCLUSIONS

We performed *WISE* and *GALEX* aperture photometry on a combined sample of 91 ETGs from Rampazzo et al. (2013) which had uniform MIR line flux measurements, and 260 ETGs from the ATLAS^{3D} survey, which have significant ancillary data. The photometric accuracy is about 0.05 mag in the MIR and 0.1 mag in the UV. We chose an identical aperture to one used by the 2MASS XSC.

The MIR is a useful wavelength region to calculate stellar masses since the effects of extinction and young stars are reduced compared to shorter wavelengths. We converted the ATLAS^{3D} $(M/L)_{stars}$ from r-band to W1 and corrected for the change in aperture between the two studies. We found that the ATLAS^{3D} M/L_{W1} measurements are significantly larger than those predicted by SPS models. We did not find a trend between M/L_{W1} and W1-W2 for old stellar populations predicted by SPS models. We obtained an average $\log M/L_{W1} = 0.07 \pm 0.13$, which is based on dynamical M/L_{W1} rather than fits to SPS models. Our color selection of dustless galaxies biases our value toward higher M/L_{W1}; but without the color-cut, we still observe a 2σ discrepancy.

Our high M/L_{W1} compared to SPS models agrees with

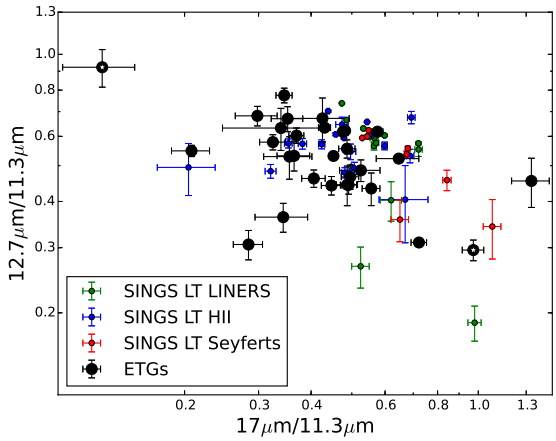

Figure 15. Plot like Fig. 9, but with 12.7 μm/11.3 μm, which arises from C—H multiplets, vs. 17 μm/11.3 μm, which arises from single C—H bonds. While there does seem to be a distinction between HII galaxies and Seyferts in the 12.7 μm/11.3 μm ratio, the ETG population is not statistically distinct from either of them. For the 17 μm/11.3 μm ratio, ETGs are similar to HII galaxies, but distinct from LINERs and Seyferts.

recent research indicating that the IMF varies, and is more Salpeter-like at high velocity dispersions. When the M/L_{W1} from our galaxies is compared to FSPS models with Chabrier (2003) and Salpeter (1955) IMFs, and we find that the dynamically-derived masses mostly fall in-between the two IMFs, mirroring the effect seen from M/L_{W1} derived from optical spectra.

We clearly identify circumstellar dust in the W3 and W4 bands for many ETGs. Surprisingly, this circumstellar dust emission appears to be ubiquitous at much greater ages than predicted by SPS models, even after accounting for potential contamination in our dustless sample. We also find that W4 emission is underpredicted by models by about a factor of 2.5. This underprediction is also seen in other SPS models.

With all-sky coverage, the *WISE* mission makes stellar mass and SFR estimates very accessible. The *WISE* W3 and W4 bands are sensitive to dust warmed by recent star formation. For objects with low sSFR, circumstellar dust emission can contaminate these tracers, leading to an inflated result. We determined that circumstellar dust contributes approximately 2×10^{-12} yr^{-1} to the sSFR signal in both W3 and W4 and we provide relations to correct for the circumstellar dust contribution to W3 and W4.

Lastly, we compared MIR spectra for spirals, LINERs, Seyferts, and ETGs in order to investigate the source of anomalous PAH ratios. We found that ETGs and Seyferts have significantly distinct 11.3 μm/7.7 μm ratios from spirals, as well as from each other. This strongly suggested that the cause of anomalous PAH ratios is more than just the presence of an AGN. The ETGs also have significantly distinct 17 μm/11.3 μm values from the LINERs and Seyferts.

Using available [S III] 18.7 μm/[S III] 33.5 μm and $H_2S(3)/H_2S(1)$ ratios, we noted that gas temperature and electron density do not correlate with the presence of anomalous PAH ratios. The incident UV flux on the PAHs also does not appear to correlate with 7.7 μm/11.3 μm ratio. Based on these results, we conclude that the anomalous PAH ratios are unlikely to be due to global variation in the ISRF.

We did not see evidence for the preferential destruction of smaller PAHs based on the 6.2 μm/7.7 μm and 8.6 μm/7.7 μm ratios. However, due to the nonuniform availability of upper limits in published line intensities, we excluded galaxies without detections. A uniform treatment of upper limits may reveal more information about small PAHs in these galaxies. We did not find evidence of dehydrogenation of small PAHs in the 12.7 μm/11.3 μm ratio.

The strongest correlation with anomalous PAH emission is the strength of shocks in H_2. We found that both ETGs and Seyferts follow this trend, although ETGs generally have more H_2 emission. Exactly how shocks bring about the anomalous emission is still largely uncertain. However, we determined from X-ray luminosities that it is likely unrelated to the activity of the central supermassive black hole.

One particularly interesting result we found was that the ETGs have 17 μm/11.3 μm ratios significantly lower than Seyferts and LINERS, but similar to spirals. This ratio is sensitive to the presence of large grains, and has been observed to trend with metallicity. Our result can be explained by the lack of the hard radiation environment found in Seyferts, or if the PAHs were accreted from an external, low-metallicity galaxy.

Finally, we attempted to use *WISE* to classify the PAH properties of ETGs. We found that *WISE* colors are only able to determine the presence of dust in ETGs, but not the MIR class. We conclude that finer distinctions are not possible because of the spectral placement of the *WISE* filters and our photometric precision. However, the W2-W3 colors may be able to inform detailed follow-up spectra of early-type galaxies in order to more efficiently calculate the prevalence of anomalous PAH ratios.

ACKNOWLEDGMENTS

GVS and PM would like to thank C. Conroy for his valuable insights into SPS models, A. Gil de Paz for helpful information about *GALEX* photometry, and J.D. Smith for useful discussions about PAHs, and the anonymous referee. GVS would also like to thank T. Jarrett for providing additional details regarding *WISE* fluxes, luminosities, masses, and SFRs for nearby galaxies. This publication makes use of data products from the *Wide-field Infrared Survey Explorer*, which is a joint project of the University of California, Los Angeles, and the Jet Propulsion Laboratory/California Institute of Technology, funded by the National Aeronautics and Space Administration. Some/all of the data presented in this paper were obtained from the Mikulski Archive for Space Telescopes (MAST). STScI is operated by the Association of Universities for Research in Astronomy, Inc., under NASA contract NAS5-26555. Support for MAST for non-*HST* data is provided by the NASA Office of Space Science via grant NNX13AC07G and by other grants and contracts. This research has made use of the NASA/IPAC Extragalactic Database (NED) which is operated by the Jet Propulsion Laboratory, California Institute of Technology, under contract with the National Aeronautics and Space Administration.

This research made use of Astropy, a community-

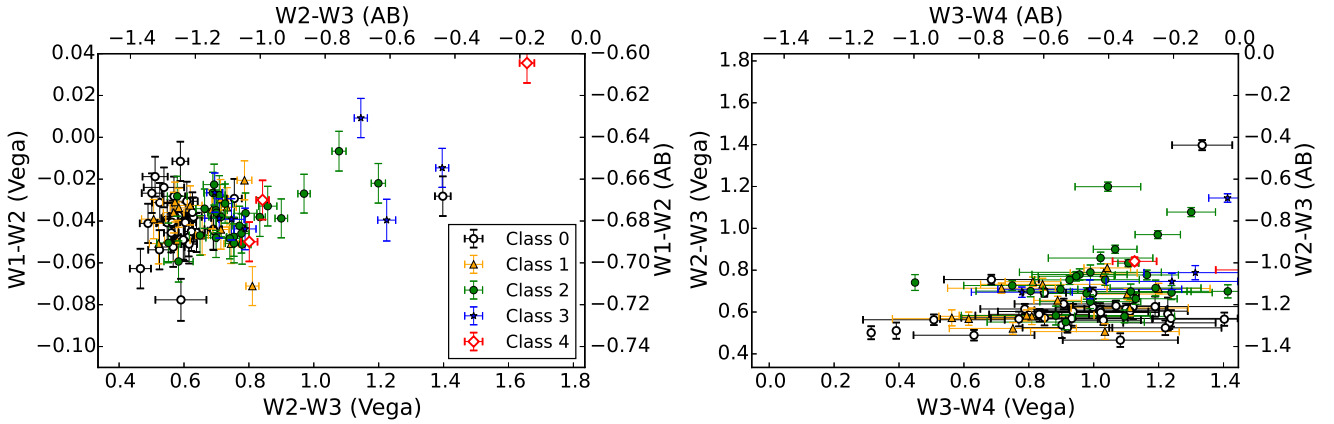

Figure 16. *Left:* W1-W2 vs. W2-W3 for the sample of galaxies in Rampazzo et al. (2013). W1-W2 is sensitive to the stellar population, so we do not see separation based on properties of the interstellar dust. W2-W3 measures the presence of PAH features compared to the stellar population. This causes the Class-0 objects separate from the Class-2-4 objects. Galaxies located off the plot are: IC 5063, NGC 1052, NGC 1275, NGC 2685, NGC 4383, and NGC 5128. *Right:* W2-W3 vs W3-W4 for the sample of galaxies in Rampazzo et al. (2013). There does not appear to be strong discrimination in W3-W4 due to the hot dust population, as seen in W2-W3. Located off the plot to the top and to the right are: all Class-4 objects, NGC 2685, NGC 3245, NGC 4383, and NGC 4435.

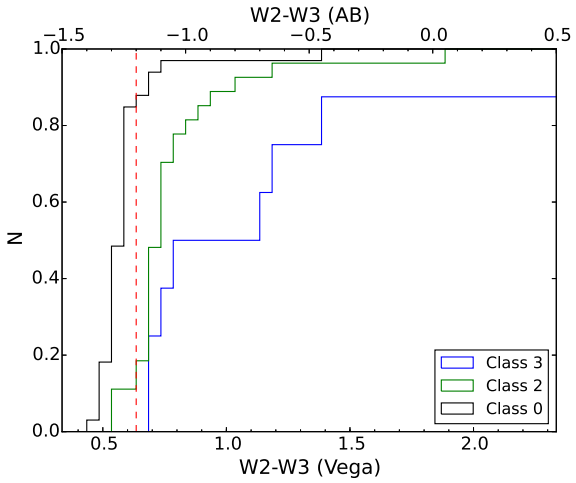

Figure 17. Cumulative histogram of the W2-W3 colors of the Class-0, Class-2, and Class-3 objects. The Class-0 objects are from a population statistically distinct from both the Class-2 and Class-3 objects. We propose a color-cut to distinguish between Class-0 and Class-2–3 objects at W2-W3=-1.2 (AB), which is denoted by the red dashed line. Class-4 objects are from a population statistically distinct from all other classes. There are no other separations which can be made using W2-W3 colors.

developed core Python package for Astronomy (Astropy Collaboration 2013). This research made use of APLpy, an open-source plotting package for Python hosted at http://aplpy.github.com. This research made use of the IPython package (Pérez & Granger 2007). IRAF is distributed by the National Optical Astronomy Observatory, which is operated by the Association of Universities for Research in Astronomy (AURA) under a cooperative agreement with the National Science Foundation. This research made use of matplotlib, a Python library for publication quality graphics (Hunter 2007). PyRAF is a product of the Space Telescope Science Institute, which is operated by AURA for NASA. This research made use of SciPy (Jones et al. 01).

REFERENCES

Abazajian K. N., et al., 2009, ApJS, 182, 543
Alatalo K., et al., 2013, MNRAS, 432, 1796
Allain T., Leach S., Sedlmayr E., 1996, A&A, 305, 602
Allamandola L. J., Tielens A. G. G. M., Barker J. R., 1989, ApJS, 71, 733
Allamandola L. J., Hudgins D. M., Sandford S. A., 1999, ApJ, 511, L115
Amblard A., Riguccini L., Temi P., Im S., Fanelli M., Serra P., 2014, ApJ, 783, 135
Astropy Collaboration et al., 2013, A&A, 558, A33
Athey A., Bregman J., Bregman J., Temi P., Sauvage M., 2002, ApJ, 571, 272
Bai Y., Zou H., Liu J., Wang S., 2015, ApJS, 220, 6
Bakes E. L. O., Tielens A. G. G. M., 1994, ApJ, 427, 822
Bedijn P. J., 1987, A&A, 186, 136
Bell E. F., de Jong R. S., 2001, ApJ, 550, 212
Bell E. F., McIntosh D. H., Katz N., Weinberg M. D., 2003, ApJS, 149, 289
Bertin E., Arnouts S., 1996, A&AS, 117, 393
Blanton M. R., Roweis S., 2007, AJ, 133, 734
Brandl B. R., et al., 2004, ApJS, 154, 188
Bregman J., Temi P., 2005, ApJ, 621, 831
Bregman J. N., Snider B. A., Grego L., Cox C. V., 1998, ApJ, 499, 670
Bregman J. N., Temi P., Bregman J. D., 2006, ApJ, 647, 265
Bressan A., Granato G. L., Silva L., 1998, A&A, 332, 135
Bressan A., Marigo P., Girardi L., Salasnich B., Dal Cero C., Rubele S., Nanni A., 2012, MNRAS, 427, 127
Bruzual G., Charlot S., 2003, MNRAS, 344, 1000
Caldwell N., 1984, PASP, 96, 287
Canizares C. R., Fabbiano G., Trinchieri G., 1987, ApJ, 312, 503
Cappellari M., 2008, MNRAS, 390, 71
Cappellari M., et al., 2011, MNRAS, 413, 813
Cappellari M., et al., 2012, Nature, 484, 485
Cappellari M., et al., 2013, MNRAS, 432, 1709

Cassarà L. P., Piovan L., Weiss A., Salaris M., Chiosi C., 2013, MNRAS, 436, 2824
Chabrier G., 2003, PASP, 115, 763
Cluver M. E., et al., 2014, ApJ, 782, 90
Conroy C., 2013, ARA&A, 51, 393
Conroy C., Gunn J. E., 2010, ApJ, 712, 833
Conroy C., Gunn J. E., White M., 2009, ApJ, 699, 486
Davis T. A., et al., 2014, MNRAS, 444, 3427
DeFrees D. J., Miller M. D., Talbi D., Pauzat F., Ellinger Y., 1993, ApJ, 408, 530
Diamond-Stanic A. M., Rieke G. H., 2010, ApJ, 724, 140
Draine B. T., Li A., 2001, ApJ, 551, 807
Draine B. T., Li A., 2007, ApJ, 657, 810
Draine B. T., Salpeter E. E., 1979, ApJ, 231, 438
Duley W. W., Williams D. A., 1981, MNRAS, 196, 269
Dwek E., Arendt R. G., 1992, ARA&A, 30, 11
Ebneter K., Davis M., Djorgovski S., 1988, AJ, 95, 422
Ferrari F., Pastoriza M. G., Macchetto F. D., Bonatto C., Panagia N., Sparks W. B., 2002, A&A, 389, 355
Ford H. A., Bregman J. N., 2013, ApJ, 770, 137
Forman W., Jones C., Tucker W., 1985, ApJ, 293, 102
Galliano F., Madden S. C., Tielens A. G. G. M., Peeters E., Jones A. P., 2008, ApJ, 679, 310
Gil de Paz A., et al., 2007, ApJS, 173, 185
Girardi L., et al., 2010, ApJ, 724, 1030
Goldreich P., Scoville N., 1976, ApJ, 205, 144
Goudfrooij P., de Jong T., 1995, A&A, 298, 784
Goudfrooij P., de Jong T., Hansen L., Norgaard-Nielsen H. U., 1994, MNRAS, 271, 833
Groves B., et al., 2012, MNRAS, 426, 892
Helou G., 1986, ApJ, 311, L33
Helou G., Lu N. Y., Werner M. W., Malhotra S., Silbermann N., 2000, ApJ, 532, L21
Ho L. C., Filippenko A. V., Sargent W. L. W., 1997, ApJS, 112, 315
Hony S., Van Kerckhoven C., Peeters E., Tielens A. G. G. M., Hudgins D. M., Allamandola L. J., 2001, A&A, 370, 1030
Hudgins D. M., Allamandola L. J., 1995, The Journal of Physical Chemistry, 99, 3033
Hunter J. D., 2007, Computing In Science & Engineering, 9, 90
Indebetouw R., et al., 2005, ApJ, 619, 931
Jarrett T. H., et al., 2011, ApJ, 735, 112
Jarrett T. H., et al., 2013, AJ, 145, 6
Joblin C., Tielens A. G. G. M., Geballe T. R., Wooden D. H., 1996, ApJ, 460, L119
Jochims H. W., Ruhl E., Baumgartel H., Tobita S., Leach S., 1994, ApJ, 420, 307
Jones A. P., Tielens A. G. G. M., Hollenbach D. J., McKee C. F., 1994, ApJ, 433, 797
Jones E., Oliphant T., Peterson P., et al., 2001–, SciPy: Open source scientific tools for Python, `http://www.scipy.org/`
Jura M., Kim D. W., Knapp G. R., Guhathakurta P., 1987, ApJ, 312, L11
Kaneda H., Onaka T., Sakon I., 2005, ApJ, 632, L83
Kaneda H., Onaka T., Sakon I., Kitayama T., Okada Y., Suzuki T., 2008, ApJ, 684, 270
Kaviraj S., et al., 2007, ApJS, 173, 619
Kelson D. D., Holden B. P., 2010, ApJ, 713, L28
Kennicutt Jr. R. C., 1998a, ARA&A, 36, 189
Kennicutt Jr. R. C., 1998b, ApJ, 498, 541
Kennicutt Jr. R. C., et al., 2003, PASP, 115, 928
Knapp G. R., Turner E. L., Cunniffe P. E., 1985, AJ, 90, 454
Knapp G. R., Guhathakurta P., Kim D.-W., Jura M. A., 1989, ApJS, 70, 329
Krajnović D., et al., 2011, MNRAS, 414, 2923
Langhoff S. R., 1996, The Journal of Physical Chemistry, 100, 2819
Lonsdale Persson C. J., Helou G., 1987, ApJ, 314, 513
MacArthur L. A., Courteau S., Bell E., Holtzman J. A., 2004, ApJS, 152, 175
Madden S. C., Vigroux L., Sauvage M., 1999, in Cox P., Kessler M., eds, ESA Special Publication Vol. 427, The Universe as Seen by ISO. p. 933
Maraston C., 2005, MNRAS, 362, 799
Maraston C., Daddi E., Renzini A., Cimatti A., Dickinson M., Papovich C., Pasquali A., Pirzkal N., 2006, ApJ, 652, 85
Marigo P., Girardi L., Bressan A., Groenewegen M. A. T., Silva L., Granato G. L., 2008, A&A, 482, 883
Marigo P., Bressan A., Nanni A., Girardi L., Pumo M. L., 2013, MNRAS, 434, 488
Martin D. C., et al., 2005, ApJ, 619, L1
Martini P., Dicken D., Storchi-Bergmann T., 2013, ApJ, 766, 121
McDermid R. M., et al., 2015, MNRAS, 448, 3484
Meidt S. E., et al., 2012, ApJ, 744, 17
Meidt S. E., et al., 2014, ApJ, 788, 144
Melbourne J., Boyer M. L., 2013, ApJ, 764, 30
Melbourne J., et al., 2012, ApJ, 748, 47
Micelotta E. R., Jones A. P., Tielens A. G. G. M., 2010, A&A, 510, A36
Morrissey P., et al., 2005, ApJ, 619, L7
Morrissey P., et al., 2007, ApJS, 173, 682
Navarro J. F., Frenk C. S., White S. D. M., 1996, ApJ, 462, 563
Norris M. A., Meidt S., Van de Ven G., Schinnerer E., Groves B., Querejeta M., 2014, ApJ, 797, 55
O'Dowd M. J., et al., 2009, ApJ, 705, 885
Ogle P., Antonucci R., Appleton P. N., Whysong D., 2007, ApJ, 668, 699
Pahre M. A., Ashby M. L. N., Fazio G. G., Willner S. P., 2004, ApJS, 154, 229
Panuzzo P., Rampazzo R., Bressan A., Vega O., Annibali F., Buson L. M., Clemens M. S., Zeilinger W. W., 2011, A&A, 528, A10
Peletier R. F., et al., 2012, MNRAS, 419, 2031
Pellegrini S., 2010, ApJ, 717, 640
Pérez F., Granger B. E., 2007, Computing in Science and Engineering, 9, 21
Phillips M. M., Jenkins C. R., Dopita M. A., Sadler E. M., Binette L., 1986, AJ, 91, 1062
Planck Collaboration et al., 2014, A&A, 571, A1
Rampazzo R., Panuzzo P., Vega O., Marino A., Bressan A., Clemens M. S., 2013, MNRAS, 432, 374
Rosenfield P., et al., 2014, ApJ, 790, 22
Rosenfield P., Marigo P., Girardi L., Dalcanton J. J., Bressan A., Williams B. F., Dolphin A., 2016, ApJ, 822, 73
Roussel H., et al., 2007, ApJ, 669, 959
Sadler E. M., 1987, in de Zeeuw P. T., ed., IAU Symposium Vol. 127, Structure and Dynamics of Elliptical Galaxies. pp 125–132
Sadler E. M., Gerhard O. E., 1985, MNRAS, 214, 177
Salim S., et al., 2007, ApJS, 173, 267
Salpeter E. E., 1955, ApJ, 121, 161
Salpeter E. E., 1974a, ApJ, 193, 579
Salpeter E. E., 1974b, ApJ, 193, 585
Sarzi M., et al., 2010, MNRAS, 402, 2187
Schlegel D. J., Finkbeiner D. P., Davis M., 1998, ApJ, 500, 525
Schutte W. A., Tielens A. G. G. M., Allamandola L. J., 1993, ApJ, 415, 397
Scott N., et al., 2013, MNRAS, 432, 1894
Serra P., et al., 2012, MNRAS, 422, 1835
Shapiro K. L., et al., 2010, MNRAS, 402, 2140
Silva L., Granato G. L., Bressan A., Danese L., 1998, ApJ, 509, 103
Smith B. J., Struck C., Hancock M., Appleton P. N., Charmandaris V., Reach W. T., 2007, AJ, 133, 791
Smith M. W. L., et al., 2012, ApJ, 748, 123

Sparks W. B., Wall J. V., Thorne D. J., Jorden P. R., van Breda I. G., Rudd P. J., Jorgensen H. E., 1985, MNRAS, 217, 87
Szczepanski J., Vala M., 1993, ApJ, 414, 646
Taylor E. N., et al., 2011, MNRAS, 418, 1587
Temi P., Brighenti F., Mathews W. G., 2009, ApJ, 695, 1
Trams N. R., et al., 1999, A&A, 346, 843
Vega O., et al., 2010, ApJ, 721, 1090
Veron-Cetty M.-P., Veron P., 1988, A&A, 204, 28
Villaume A., Conroy C., Johnson B. D., 2015, ApJ, 806, 82
Wardle M., Knapp G. R., 1986, AJ, 91, 23
Weingartner J. C., Draine B. T., 2001, ApJS, 134, 263
Wright E. L., et al., 2010, AJ, 140, 1868
Xilouris E. M., Madden S. C., Galliano F., Vigroux L., Sauvage M., 2004, A&A, 416, 41
Yi S. K., et al., 2005, ApJ, 619, L111
Young L. M., et al., 2011, MNRAS, 414, 940
Zibetti S., Charlot S., Rix H.-W., 2009, MNRAS, 400, 1181
di Serego Alighieri S., et al., 2013, A&A, 552, A8
van Dokkum P. G., Conroy C., 2012, ApJ, 760, 70
van Loon J. T., Groenewegen M. A. T., de Koter A., Trams N. R., Waters L. B. F. M., Zijlstra A. A., Whitelock P. A., Loup C., 1999, A&A, 351, 559